



HAL
open science

Three-dimensional Martian ionosphere model: II. Effect of transport processes due to pressure gradients

Jean-Yves Chaufray, F. Gonzalez-Galindo, François Forget, M. Lopez-Valverde, François Leblanc, Ronan Modolo, Sebastien Hess, Manabu Yagi, P.-L. Blelly, Olivier Witasse

► To cite this version:

Jean-Yves Chaufray, F. Gonzalez-Galindo, François Forget, M. Lopez-Valverde, François Leblanc, et al. Three-dimensional Martian ionosphere model: II. Effect of transport processes due to pressure gradients. *Journal of Geophysical Research. Planets*, 2014, 119 (7), pp.1614-1636. 10.1002/2013JE004551 . hal-01010734

HAL Id: hal-01010734

<https://hal.science/hal-01010734>

Submitted on 18 Sep 2020

HAL is a multi-disciplinary open access archive for the deposit and dissemination of scientific research documents, whether they are published or not. The documents may come from teaching and research institutions in France or abroad, or from public or private research centers.

L'archive ouverte pluridisciplinaire **HAL**, est destinée au dépôt et à la diffusion de documents scientifiques de niveau recherche, publiés ou non, émanant des établissements d'enseignement et de recherche français ou étrangers, des laboratoires publics ou privés.

RESEARCH ARTICLE

10.1002/2013JE004551

Key Points:

- Three-dimensional GCM-Ionosphere model
- Effects of pressure gradients on the vertical and horizontal ions density
- Diurnal, seasonal, and solar activity variations of the Martian ionosphere

Correspondence to:

J.-Y. Chaufray,
chaufray@latmos.ipsl.fr

Citation:

Chaufray, J.-Y., F. Gonzalez-Galindo, F. Forget, M. Lopez-Valverde, F. Leblanc, R. Modolo, S. Hess, M. Yagi, P.-L. Blelly, and O. Witasse (2014), Three-dimensional Martian ionosphere model: II. Effect of transport processes due to pressure gradients, *J. Geophys. Res. Planets*, 119, 1614–1636, doi:10.1002/2013JE004551.

Received 2 OCT 2013

Accepted 16 JUN 2014

Accepted article online 19 JUN 2014

Published online 21 JUL 2014

Three-dimensional Martian ionosphere model: II. Effect of transport processes due to pressure gradients

J.-Y. Chaufray^{1,2}, F. Gonzalez-Galindo³, F. Forget¹, M. Lopez-Valverde³, F. Leblanc⁴, R. Modolo⁴, S. Hess⁴, M. Yagi^{4,5}, P.-L. Blelly⁶, and O. Witasse⁷

¹Laboratoire de Météorologie Dynamique, Paris, France, ²Now at LATMOS, Guyancourt, France, ³Instituto de Astrofísica de Andalucía, CSIC, Granada, Spain, ⁴Laboratoire Atmosphere, Milieux et Observations Spatiales, Guyancourt, France, ⁵Now at PPARC, Tohoku University, Sendai, Japan, ⁶Institut de Recherche en Astrophysique et Planétologie, Toulouse, France, ⁷ESA/ESTEC, Noordwijk, Netherlands

Abstract To study the transport of the ionospheric plasma on Mars, we have included a 3-D multifluid dynamical core in a Martian general circulation model. Vertical transport modifies the ion density above ~160 km on the dayside, especially the ions produced at high altitudes like O⁺, N⁺, and C⁺. Near the exobase, the dayside to nightside flow velocity reaches few hundreds of m/s, due to a large horizontal pressure gradient. Comparison with Mars Express/Analyzer of Space Plasmas and Energetic Atoms-3 measurements between 290 and 500 km suggests that this flow could account for at least 20% of the flow produced by the solar wind. This flow is not sufficient to populate substantially the nightside ionosphere at high altitudes, in agreement with recent observations, because of a strong nightside downward flow produced by vertical pressure gradient. The O₂⁺ and NO⁺ ion densities on the nightside at low altitudes (~130 km) are modified by this downward flow, compared to simulated densities without ion dynamics, while other ions are lost by chemical reactions. Variability at different time scales (diurnal, seasonal, and solar cycles) are studied. We simulate diurnal and seasonal variations of the ionospheric composition due to the variability of the neutral atmosphere and solar flux at the top of the atmosphere. The ionospheric dynamics are not strongly affected by seasons and solar cycles, and the retroaction of the ionosphere on the neutral atmosphere temperature and velocity is negligible compared to other physical processes below the exobase.

1. Introduction

The Martian ionosphere was first observed by radio occultation with the Mariner 4 spacecraft in 1965 [Fjeldbo and von Eshleman, 1968]. The composition of the ionosphere was measured later by retarding potential analyzers during the Viking 1 and 2 descents [Hanson et al., 1977]. Recent reviews on the Martian ionosphere can be found in Nagy et al. [2004], Gurnett et al. [2008], Witasse et al. [2008], and Withers [2009]. The recent observations of the Martian ionosphere by Mars Global Surveyor (MGS) and Mars Express missions have strongly increased our knowledge of the structure of the Martian dayside ionosphere with an unprecedented amount of electron density profiles. Reviews of these observations are given in Gurnett et al. [2008], Withers [2009], Haider et al. [2011], and Withers et al. [2012a]. The solar zenith angle (SZA) variations of the electron density at the peak altitude and scale height above the peak are well described by the Chapman theory [Němec et al., 2011a; Sánchez-Cano et al., 2013; Girazian and Withers, 2013]. Two other peaks are sometimes observed at lower altitudes, a secondary peak due to the X-ray absorption, whose altitude is anticorrelated with solar activity [Fox and Weber, 2012], and a more sporadic peak due to meteoritic impact [Pätzold et al., 2005]. Seasonal variations of the main peak altitude have been observed from the Radio Science experiment on MGS [Zou et al., 2011], and Mars Advanced Radar for Subsurface and Ionosphere Sounding (MARSIS) on Mars Express [Morgan et al., 2008] in agreement with 3-D models [Bougher et al., 2000; González-Galindo et al., 2013]. These ionospheric variations are consistent with the seasonal variations of the neutral density obtained by accelerometer measurements [Keating et al. 2008] or observed by Spectroscopy for Investigation of Characteristics of the Atmosphere of Mars/Mars Express at a given altitude and predicted by the Laboratoire de Météorologie Dynamique (LMD)-Global circulation model [Forget et al., 2009] and Mars General Circulation Model and Mars-Thermosphere General Circulation Model (MGCM-MTGCM) model [McDunn et al., 2010]. A sporadic and weak nightside ionosphere was observed by the Viking mission [Zhang et al., 1990] and also by

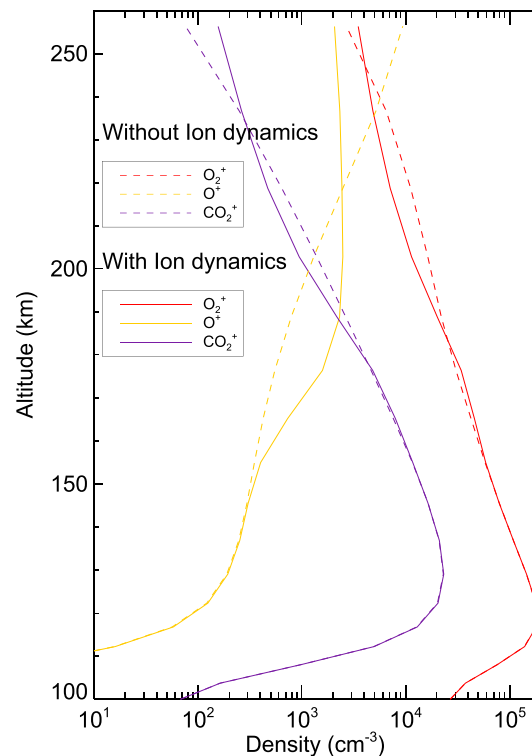


Figure 1. Comparison of computed density profiles of O_2^+ (red), O^+ (yellow), and CO_2^+ (blue) above the subsolar point with the ion dynamics (solid lines) and without ion dynamics (dashed lines). All the profiles are averaged over one Martian rotation at $L_s = 0^\circ$ for solar average conditions.

the Radio Science experiment Mars Radio Science Experiment (MaRS) on Mars Express and was attributed to transport from dayside to nightside for SZA lower than 115° and from electron precipitations at larger SZA [Duru et al., 2011; Némec et al., 2011b; Withers et al., 2012b]. Densities of most of the ions produced on the dayside decrease rapidly on the nightside due to recombination of molecular ions or charge exchange followed by recombination for atomic ions. A recent 3-D ionospheric model shows that NO^+ ions have a chemical lifetime long enough to populate the Martian nightside and could be the dominant ion on the nightside at low altitudes [González-Galindo et al., 2013].

Above 180 km, transport processes can affect the plasma densities [Shinagawa and Cravens, 1989, 1992; Fox, 1997; Krasnopolsky, 2002; Némec et al., 2011a; Mendillo et al., 2011]. Contrary to Earth, on Mars and Venus, the ionosphere is the obstacle of the solar wind and can freely respond to plasma pressure gradients due to the absence of a strong internal magnetic field. At high altitudes, the ionosphere directly interacts with the solar wind [Ma et al., 2004] and the effects of induced magnetic field are important. A transition between the ionosphere and the magnetosheath plasma, the ionopause, characterized by a strong density gradient, is sometimes observed at 400–500 km [Duru et al.,

2009; Gurnett et al., 2010]. Additionally, large fluctuations of the electron density have been observed close to this altitude, associated with large magnetic field fluctuations. These large magnetic field fluctuations are produced by solar wind and magnetosheath plasma perturbations [Gurnett et al., 2010]. Moreover, the dynamic processes driven by the solar wind interaction are likely to produce additional transient electron density peaks above 200 km [Kopf et al., 2008].

Recent observations by several Mars Express instruments suggest that dynamics of the ionosphere may play an important role in the structure of the upper ionosphere and the plasma escape processes [Lundin et al., 2008; Fränz et al., 2010]. Supersonic trans terminator flows reaching velocities ~ 5 km/s between 250 and 500 km altitude were derived from ion mass analyzer (IMA)-Analyzer of Space Plasmas and Energetic Atoms (ASPERA) on Mars Express [Fränz et al., 2010]. Such supersonic flows were also observed on Venus by the retarding potential analyzer (ORPA) on Pioneer Venus Orbiter (PVO) [Miller and Whitten, 1991]. Miller and Whitten [1991] show that the ionosphere of Venus was horizontally divided into three regions (see their Figure 1): (1) The dayside region with slow velocity and ion density decreasing monotonically with increasing solar zenith angle, (2) The terminator region ($80^\circ < SZA < 110^\circ$) or transition region with the highest ion velocities close to the thermal velocity, and (3) The nightside region where the flow slows and becomes chaotic.

Finally, the composition and the plasma temperatures of the Martian ionosphere are still poorly studied, because the instruments dedicated to the study of the Martian ionosphere are not able to derive them, and only Viking measurements are available. The NASA mission, Mars Atmosphere and Volatile Evolution (MAVEN), is expected to provide a better picture of the global composition, dynamics and energy of the Martian ionosphere, and the use of Martian ionospheric models should be useful to interpret local observations.

Several models have been developed to study the Martian ionosphere. Nagy et al. [2004] review the first models developed to understand the Martian ionosphere and its interaction with the solar wind. Here we only consider the most recent developments. One-dimensional models have been used to solve the

photodiffusion equation of several ions and electrons in the Martian upper atmosphere [Krasnopolsky, 2002; Fox, 2003; Mendillo *et al.*, 2011] to simulate ion density variations with altitude. These models simulate major and minor ions including a large set of chemical reactions. They have been used to study the effects of an ionospheric outflow on the ion density profiles [Fox, 1997]. This author derives the maximum rates of the ion escape and suggests that O_2^+ could be the major escaping ion if all ions are escaping at their maximum rates. First detection of molecular hydrogen in the Martian thermosphere [Krasnopolsky and Feldman, 2001] led to studies of the effects of H_2 -ion chemistry by several 1-D models [Krasnopolsky, 2002; Fox, 2003; Matta *et al.*, 2013], showing the importance of H_2 in accurately describing the Martian ionospheric composition. These models show that HCO_2^+ , HCO^+ , and OH^+ could be important ions in the Martian ionosphere. In these models, the neutral temperature is parametrized, and neutral densities can be derived from diffusive equilibrium assumptions [Mendillo *et al.*, 2011], or from including both diffusion and chemistry for minor species [Fox, 2003], or from including both diffusion and chemistry for all species [Krasnopolsky, 2002]. These models have also investigated the effects of enhanced soft X-ray flux on the Martian ionosphere [Fox, 2004] as well as the effects of solar cycle variability [Krasnopolsky, 2002].

Electron transport models have also been used to study the effect of precipitating electrons on the Martian ionosphere [e.g., Fox and Dalgarno, 1979; Haider *et al.*, 1992; Nicholson *et al.*, 2009; Fillingim *et al.*, 2010]. These models study the excitation, ionization, and heating of the upper Martian atmosphere resulting from electron precipitations at the dayside, nightside, or above crustal field regions.

Global models of the solar wind/Mars interaction have been used to simulate the magnetic boundaries observed in the Martian plasma environment. These models can be divided in two categories: fluid models that solve the MHD or multifluid equations and hybrid models that use a kinetic approach. The main current models have been compared in Brain *et al.* [2010, and references therein]. The spatial resolution of these models has been reduced to describe the Martian ionosphere. Because these models describe consistently the solar wind interaction with the ionosphere, they do not require any arbitrary upper limit boundary. However, in their current version, these models include only few chemical reactions needed to describe the major ions of the Martian ionosphere (O_2^+ , CO_2^+ , O^+ , and H^+), and the neutral atmosphere is fixed. These models have been intensively used to study the ion escape rates at Mars, and their densities over several planetary radii. More recently, these models have been used to study the composition of the Martian ionosphere and the effects of the magnetic crustal field [Ma *et al.*, 2004; Najib *et al.*, 2011; Brecht and Ledvina, 2012]. Ma *et al.* [2004] show that upward transport was important above magnetic crustal field regions.

Finally, recent developments of the 3-D thermospheric model such as MTGCM [Bougher *et al.*, 2004] and LMD-general circulation model (GCM) [González-Galindo *et al.*, 2013] have incorporated neutral photoionization and ion-neutral chemistry to simulate the Martian ionosphere at altitudes where photoequilibrium assumption is valid (below ~ 180 km at dayside). In this paper we present a 3-D model of the Martian ionospheric dynamics added to a general circulation model (GCM). Contrary to the other 3-D models, our model does not describe the solar wind interaction with the ionosphere, but includes consistently the ionosphere/atmosphere coupling and a larger set of chemical reactions, as well as neutral winds and planetary rotation. The importance of the neutral/ionosphere coupling has been shown by Bougher *et al.* [2004] from MGS Radio Science observations.

A first model of the Martian ionosphere, neglecting transport processes, has been presented by González-Galindo *et al.* [2013]. These authors validate the model, by comparing numerous Mars Global Surveyor observations and simulations of the ionospheric peak density and altitude. In this study, we will focus on the effects of the pressure gradients on the upper part of the ionosphere and on its composition. Given the lack of a large number observations, and because a GCM is adapted to describe average conditions derived from numerous observations, we do not try to fit the Viking 1 and 2 observations. However, the comparison shows a reasonable agreement with differences that are basically understood. MAVEN should provide a larger set of observations of ionospheric composition, which we will use to make a systematic comparison between simulations and observations to validate our model. Induced and crustal magnetic fields could play an important role in the dynamics of the upper atmosphere [Fillingim *et al.*, 2012] and their effects will be investigated in the future. In this paper, we focus on the horizontal and vertical pressure

gradients and their effects on Martian ionospheric dynamics. Observations of the ionosphere of Venus show that, depending on upstream solar wind conditions, the ionosphere can be magnetized or unmagnetized [Luhmann and Cravens, 1991]. On Mars, the situation is less clear [Dubinin *et al.*, 2008], and observations of the dayside ionosphere from MaRS show a variable and complex vertical structure of the topside ionosphere, with single, double, or sometimes triple scale heights [Withers *et al.*, 2012a], which could result from a change of mechanism controlling the plasma dynamics or a change in the ionospheric parameters (composition, plasma temperature, etc.) [Withers *et al.*, 2012a]. Therefore, the unmagnetized assumption used here is not for all upstream conditions. In the next section, the GCM and especially the physics of the upper atmosphere included in the model are described as well as the mathematical and numerical approach used to solve time-dependent equations of the ionospheric dynamics. Comparisons with other models and Viking observations are done in the third section. In the fourth section, the vertical and horizontal variations of the density of the major ions are described and discussed, and finally, the seasonal and solar activity variations are described and discussed in the fifth section. Future works and a discussion about the processes not included are presented in the last section.

2. Model Description

2.1. GCM Model

The LMD-MGCM model is an extension of the model described by Forget *et al.* [1999] to the thermosphere. It has been described by Angelats i Coll *et al.* [2005] and detailed in González-Galindo *et al.* [2009a, 2009b]. The model is composed of a “dynamical core” solving the continuity, momentum, and energy equation of the Martian atmosphere and a “physical core” solving the sources and loss terms, and the subgrid processes, such as turbulence in the planetary boundary layer, convection, subgrid-scale orography (see Forget *et al.* [1999] for details). This model was used to generate the Martian Climate Database [Lewis *et al.*, 1999]. The atmosphere is assumed to be in hydrostatic equilibrium. Horizontal dynamics is solved on a vertical “hybrid” η grid, equivalent to a $\sigma = P/P_s$ coordinate at low altitudes ($< \sim 50$ km) and Pressure P coordinate at high altitudes ($> \sim 50$ km), where P is the local pressure and P_s is the surface pressure at the same latitude and longitude [Forget *et al.*, 2007; González-Galindo *et al.*, 2009a]. The horizontal grid is a 64×48 regular grid point corresponding to 3.75° latitude by 5.625° longitude. The horizontal dynamics equation is solved to compute the zonal and meridional components of the atmospheric velocity. The vertical velocity is derived from integration of the continuity conservation equation [Hourdin, 2005]. The physical parametrization of the different processes included in the physical core have been described in Forget *et al.* [1999]. Since then, the model has been improved by including the following: the variations of water vapor at different spatial scales and timescales [e.g., Montmessin *et al.*, 2005], photochemical reactions in the Martian mesosphere to describe ozone [Lefevre *et al.*, 2004] and methane [Lefevre and Forget, 2009], improvement of dust and cloud effects on radiative transfer [Madeleine *et al.*, 2011], and coupling with a mesoscale model to describe the atmosphere-surface interactions at mesospatial scale [Spiga and Forget, 2009]. The model has been adapted to describe past conditions including inclination variations of the axis of Mars [Forget *et al.*, 2006] and a thicker CO_2 atmosphere [Forget *et al.*, 2013; Woodsworth *et al.*, 2012]. The upper boundary of the LMD-MGCM has also been moved up to the exobase [Angelats i Coll *et al.*, 2004, 2005; González-Galindo *et al.*, 2005, 2009a] and extended to study the ionosphere by including photoionization and photoelectron impact processes [González-Galindo *et al.*, 2013], and incorporates a new molecular diffusion and CO_2 $15 \mu\text{m}$ Nonlocal Thermodynamic Equilibrium cooling scheme (M. A. López-Valverde *et al.*, manuscript in preparation, 2014; J.-Y. Chaufray *et al.*, Variability of the hydrogen in the Martian upper atmosphere as simulated by a 3D Atmosphere-Exosphere coupling, submitted to *Icarus*, 2014). A coupling between this model and an exospheric model describing the thermal and suprathermal oxygen populations in the Martian exosphere was done by Yagi *et al.* [2012] to investigate the seasonal variability of the hot oxygen escape flux.

2.2. Physical Model

In this study, we use the same set of photochemical reactions presented in González-Galindo *et al.* [2013]. Contrary to González-Galindo *et al.* [2013] who neglected the differential ion and neutral transport processes, we include an ambipolar diffusion in the ionosphere but neglect the ionospheric currents. This latter approximation is probably not fulfilled above strong crustal field regions as well as in regions of strong ionospheric currents [Fillingim *et al.*, 2010], and such effects will be studied in the next years. The

results presented here should be valid in the case of weak ionospheric currents and regions outside the crustal fields.

The diffusion assumption is generally used to describe the vertical structure of unmagnetized ionospheres [Krasnopolsky, 2002; Mendillo *et al.*, 2011; Fox and Weber, 2012]. Ma *et al.* [2004], in their 3-D model of the Martian ionosphere-magnetosphere, assume that ions and electrons have the same velocity and therefore neglect both horizontal and vertical ionospheric currents. In a diffusion assumption, the polarization electric field is driven by the electrons creating a slight charge separation [Schunk and Nagy, 2009]. This polarization electric field acts on the ions to move them with the electrons and therefore must be included to describe ion dynamics. This slight charge separation occurs on a typical distance equal to the electron Debye length (few centimeters) which is much smaller than the GCM spatial step (few kilometers), so we assume electroneutrality.

Due to the very different vertical spatial scale, the vertical and horizontal dynamics equations are solved separately. The vertical stratification of the ionosphere is steeper than the horizontal stratification and therefore vertical pressure gradients are assumed to be much larger than inertial terms. Only ion-neutral collisions are included in the ion dynamics equations. Ion-ion collisions could change the ion density in the upper atmosphere by 15–75% [Matta *et al.*, 2013] which is much lower than the diurnal and seasonal variations presented below. Some possible important species such as HO^+ and HCO^+ resulting from ions-hydrogen chemistry [Fox, 2003; Matta *et al.*, 2013] are not included in the current version. These species have not been observed yet and therefore their densities are not constrained. In the current model, we assume that $\Delta T_e = (T_e - T_n)$ and $\Delta T_k = (T_k - T_n)$, where T_n is the neutral atmosphere temperature, T_e is the electron temperature, and T_k is the temperature of ion k , are constant and uniform on an isobar surface. We use temperature profiles from Fox and Bakalian [2001], based on Viking measurements [Hanson *et al.*, 1977; Hanson and Mantas, 1988] and calculations of Rohrbaugh *et al.* [1979]. The values of these temperatures are difficult to improve due to the lack of measurements of ion and electron temperatures. A way to improve the model would be to solve the energy equation of ions and electrons which requires the addition of several processes such as heat transfer from freshly created photoelectrons to ambient electrons or conductive heating transport. Such an improvement will be done when the MAVEN/Langmuir Probe and Waves measurements of electron temperatures become available. All the simulations presented here have been done over one Martian rotation, the current model that includes transport processes is computationally intensive to simulate a full Martian year as González-Galindo *et al.* [2013] have done.

2.3. Mathematical Model

The fundamental equations [see Schunk and Nagy, 2009] solved by the model include the continuity equation (equation (1)), horizontal and vertical dynamics equations (equations (2a) and (2b)) for each ion.

$$\frac{\partial \rho_k}{\partial t} + \nabla_{\mathbf{H}} \cdot [\rho_k \mathbf{u}_{\mathbf{n}}] + \frac{\partial \rho_k w_n}{\partial z} + \nabla_{\mathbf{H}} \cdot [\rho_k (\mathbf{u}_{\mathbf{k}} - \mathbf{u}_{\mathbf{n}})] + \frac{\partial \rho_k (w_k - w_n)}{\partial z} = S_k - L_k \quad (1)$$

$$\frac{\partial \mathbf{u}_{\mathbf{k}}}{\partial t} + w_k \frac{\partial \mathbf{u}_{\mathbf{k}}}{\partial z} + (\zeta_{\mathbf{k}} + 2\mathbf{\Omega}) \times \mathbf{u}_{\mathbf{k}} + \nabla_{\mathbf{H}} \left(\frac{u_{\mathbf{k}}^2}{2} \right) = -v_{kn} (\mathbf{u}_{\mathbf{k}} - \mathbf{u}_{\mathbf{n}}) - \frac{1}{\rho_k} \nabla_{\mathbf{H}} P_k + \frac{Z_k e}{m_k} \mathbf{E}_{\mathbf{H}} \quad (2a)$$

$$0 = -v_{kn} (w_k - w_n) - \frac{1}{\rho_k} \frac{\partial P_k}{\partial z} + \frac{Z_k e}{m_k} E_z - g \quad (2b)$$

where t is the time ρ_k is the mass density of ion k , $\mathbf{u}_{\mathbf{n}}$ and w_n are the horizontal and vertical neutral velocities, and $\mathbf{u}_{\mathbf{k}}$ and w_k are the horizontal and vertical ion velocity. $\nabla_{\mathbf{H}}$ refers to horizontal gradient operator and z is the altitude. S_k and L_k are the source and loss terms of ion k . All boldface font indicates vector quantities. The left part of equation (2a) represents the inertia terms. These inertia terms are negligible compared to the strong pressure gradients on the vertical dynamics (2b).

The ionospheric vorticity and planetary rotation vector are $\zeta_{\mathbf{k}} = \nabla \times \mathbf{u}_{\mathbf{k}}$ and $\mathbf{\Omega}$. Only their component along the local vertical z is considered as done in the neutral dynamics [Hourdin, 2005]. This is a traditional simplification done to compute the neutral dynamics and that we use also to describe the ion dynamics. Horizontal components of these terms involve vertical movements which are negligible in our model. The ion-neutral collision frequency is v_{kn} , P_k the partial pressure of the ion k , $\mathbf{E}_{\mathbf{H}}$ and E_z the horizontal and

vertical components of the electric field (see below), Z_k and m_k the atomic number and mass of the ion k , respectively, and e and g are the charge unit and the acceleration due to gravity, respectively.

$$\mathbf{E}_H = -\frac{m_e}{e} \left[\frac{1}{\rho_e} \nabla_H P_e \right] \quad (3a)$$

$$E_z = -\frac{m_e}{e} \left[\frac{1}{\rho_e} \frac{\partial P_e}{\partial z} \right] \quad (3b)$$

For all ions considered in this study, $Z_k=1$ and g are considered constant in the whole atmosphere.

In the continuity equation, advection terms are split into two components: those due to atmospheric motion (second and third terms on the left side of equation (1)), and those due to ionospheric motion in the atmospheric frame (fourth and fifth terms on the left side of equation (1)). We also split the advection terms in the momentum equation (second term on the left side of equations (2a) and (2b)) into atmospheric and ionospheric contributions.

Not all ions included in the GCM are dynamically described in this study, we will only consider O_2^+ , O^+ , C^+ , N^+ , CO_2^+ , and NO^+ . O_2^+ , O^+ , and CO_2^+ are dominant ions on the dayside [e.g., *Krasnopolsky, 2002*], while NO^+ is probably the dominant ion on the nightside [*González-Galindo et al., 2013*]. C^+ and N^+ would become dominant ions in the upper ionosphere if they were not described dynamically. H^+ , N_2^+ , and CO^+ are minor ions in the Martian ionosphere below the exobase and a dynamical description of these ions should not change the results presented in this paper. Electron dynamics equations are used to derive the horizontal and vertical components of the ambipolar electric field (equations (3a) and (3b)).

Using equation (3b), the vertical dynamics equation of ions can be rewritten into the usual diffusion equation (equation (4))

$$0 = -v_{kn}(w_k - w_n) - \frac{1}{\rho_k} \frac{\partial P_k}{\partial z} - \frac{Z_k m_e}{m_k} \frac{1}{\rho_e} \frac{\partial P_e}{\partial z} - g \quad (4)$$

Finally, the electron density and velocity are computed from electroneutrality equation (equation (5)) and charge conservation (equations (6a) and (6b)).

$$\rho_e = \sum_{k=1}^{k=K} Z_k \frac{m_e}{m_k} \rho_k \quad (5)$$

$$\rho_e u_e = \sum_{k=1}^{k=K} Z_k \frac{m_e}{m_k} \rho_k u_k \quad (6a)$$

$$\rho_e w_e = \sum_{k=1}^{k=K} Z_k \frac{m_e}{m_k} \rho_k w_k \quad (6b)$$

The sum is taken over all $K=9$ ions, including the ions not described dynamically.

2.4. Numerical Model

We describe succinctly the numerical methods used to solve ion dynamics, more details are given in Appendix A.

The continuity equation (equation (1)) can be rewritten under the following form:

$$\delta \rho_k = \sum_p \left(\frac{\delta \rho_k}{\delta t} \right)_p \delta t \quad (7)$$

where $(\delta \rho_k / \delta t)_p$ is the term due to the process p . The different processes (horizontal and vertical atmospheric advection, horizontal and vertical plasma advection, and production and loss due to chemical reactions) are computed with different time steps. In the simulations presented here, the time step for atmospheric dynamics is 1/1920 of one Martian day (~ 45 s), while the time step for ionospheric horizontal dynamics is ~ 0.45 s. Ionospheric vertical transport is computed every 45 s with a subtime step varying from 0.1 to 5 s. Processes included in the physical core such as photochemistry and neutral molecular diffusion are computed every 7.5 min, with a subtime step dependent on the physical process. Horizontal and vertical

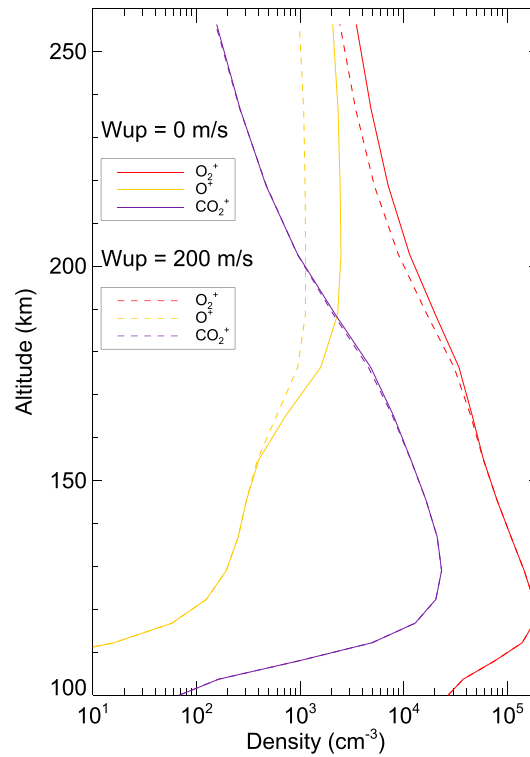


Figure 2. Comparison of the computed density profiles of O_2^+ (red), O^+ (yellow), and CO_2^+ (blue) above the subsolar point with ion dynamics assuming no vertical velocity at the top boundary (solid lines) and a vertical velocity at the top equal to 200 m/s for all ions (dashed lines). All the profiles are averaged over one Martian rotation at $L_s = 0^\circ$ for solar average conditions.

plasma advections are separated as done, for example; by *Ridley et al.* [2006] to model the Earth's ionosphere. The atmospheric and horizontal ionospheric advection terms in the continuity equations are computed using the algorithm presented by *Hourdin and Armengaud* [1998]. The computation of the chemical terms is described in *González-Galindo et al.* [2005].

The horizontal ionospheric dynamics equation (2a) is solved above $P \sim 5 \times 10^{-5}$ Pa (~ 125 – 135 km) using a grid point dynamic algorithm [*Sadouny and Laval*, 1984; *Forget et al.*, 1999]. Below this pressure level, we assume ion and electron velocities are equal to the neutral atmospheric velocity: $u_k = u_n$ and $v_k = v_n$ for all ions k . At high latitude, a filter is applied near the singularity in the grid at the pole to avoid numerical instabilities. Numerical dissipation schemes, similar to the dissipation schemes used for atmospheric dynamics [*Forget et al.*, 1999] are also applied to damp numerical instabilities occurring at regions with strong density gradients.

The zonal (meridional) velocity and electric field components are defined on a specific staggered grid in the zonal (meridional) direction according to the C grid in *Arakawa and Lamb* [1977] classification. The zonal resolution is 5.625° and the meridional resolution is 3.75° .

The numerical scheme used to solve these equations is similar to the solver of horizontal dynamics of the neutral atmosphere [*Hourdin*, 2005] and is detailed in Appendix A. Periodicity is assumed in longitude and the ion zonal velocity is equal to 0 at the poles.

Vertical ionospheric advection in the atmospheric frame (equation (8)) is solved by replacing $(w_k - w_n)$ by its expression given by equation (4) leading to equation (9) [*Shinagawa and Cravens*, 1989].

$$\left(\frac{\delta \rho_k}{\delta t}\right) = -\frac{\partial \rho_k (w_k - w_n)}{\partial z} \quad (8)$$

$$\left(\frac{\delta \rho_k}{\delta t}\right) = \frac{\partial}{\partial z} \left\{ D_k \left(\frac{\partial \rho_k}{\partial z} + \rho_k \left[\frac{1}{T_k} \frac{\partial (T_k + T_e)}{\partial z} + \frac{T_e}{T_k} \frac{1}{\rho_e} \frac{\partial \rho_e}{\partial z} + \frac{1}{H_k} \right] \right) \right\} \quad (9)$$

where $D_k = k_B T_k / m_k \nu_{kn}$ is the diffusion coefficient of the ion, k_B is the Boltzmann constant, and $H_k = k_B T_k / m_k g$ is a scale height. This equation is similar to the diffusion equation solved by *Mendillo et al.* [2011]. Contrary to horizontal dynamics, equation (9) is solved on an altitude vertical grid and not a pressure vertical grid as for the neutral diffusion scheme for which the use of the altitude grid leads to a better description of some light species. To solve it, we use a finer vertical resolution above pressure level $P_0 = 7 \times 10^{-4}$ Pa (~ 105 – 115 km). The spatial resolution is not constant because, we choose 28 grid points along the vertical and the altitude of the first and last pressure levels are not constant. Typical vertical resolution (for a lower level at 110 km and upper level at 250 km) is 5 km.

Equation (9) is nonlinear due to the term involving the electron density. We use a forward-backward (predictor-corrector) scheme to solve it. A first estimate of the ion density $\rho_k(t + dt)$ is computed using the electron density $\rho_e(t)$. An intermediate electron density $\rho_e(t + dt)$ is then computed using electroneutrality (equation (5)) and in a backward step, this value is used to solve again equation (9). The final $\rho_k(t + dt)$ and resulting $\rho_e(t + dt)$ are computed. During both forward and backward steps, the equation becomes linear in ρ_k

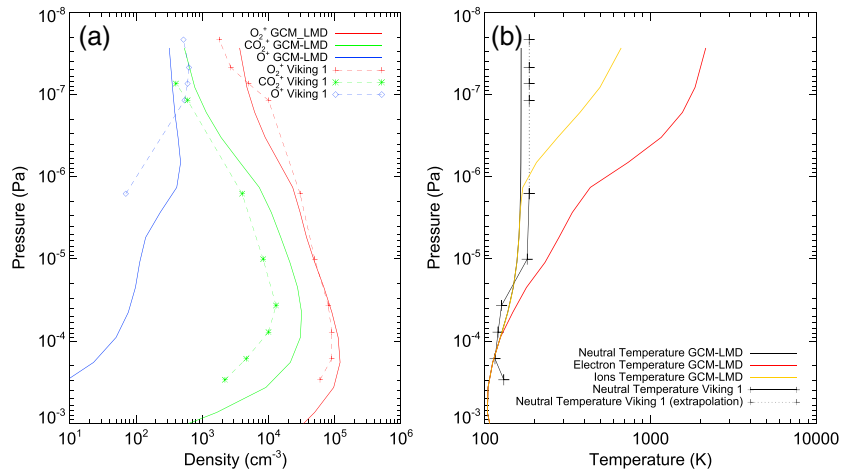


Figure 3. (a) Comparison of the computed density profiles of O₂⁺ (red line), O⁺ (blue line), and CO₂⁺ (green line) with Viking Lander 1 O₂⁺ (red crosses), O⁺ (blue diamonds), and CO₂⁺ (green stars) measured values. Profiles correspond to Viking 1 latitude and local time, Ls = 90°, for low solar conditions. All the computed profiles are averaged over one Martian rotation. (b) Comparison of the computed neutral temperature with the neutral temperature derived from Viking 1. Computed ions and electron temperatures are also indicated for information.

and a usual matrix inversion method is used to solve it, similarly to what is done to describe the *F* region of the Earth atmosphere [Schunk and Nagy, 2009, Appendix O]. Because this scheme is not fully implicit, we need a small time step to avoid numerical instabilities. A variable time step is used, dependent on the vertical velocity computed at each time step. Typical time steps are 0.1–5 s, at least 1 order of magnitude lower than the typical ionospheric time scale $t_k = H_k/w_k$. The vertical velocity of each ion at the upper boundary is a free parameter chosen equal to 0 km/s for most of the simulations presented here (diffusive equilibrium). This assumption is discussed in section 3.1. A better description of this boundary condition could be derived from a model describing the solar wind interaction with the Martian ionosphere [e.g., Modolo et al., 2005; Najib et al., 2011; Brecht and Ledvina, 2012]. We assume $w_k = w_n$ and therefore $(\delta\rho_k/\delta t)_{dyn} = 0$ (equation (8)) for each ion *k* at the lower boundary (photochemical equilibrium). We assume no ions and

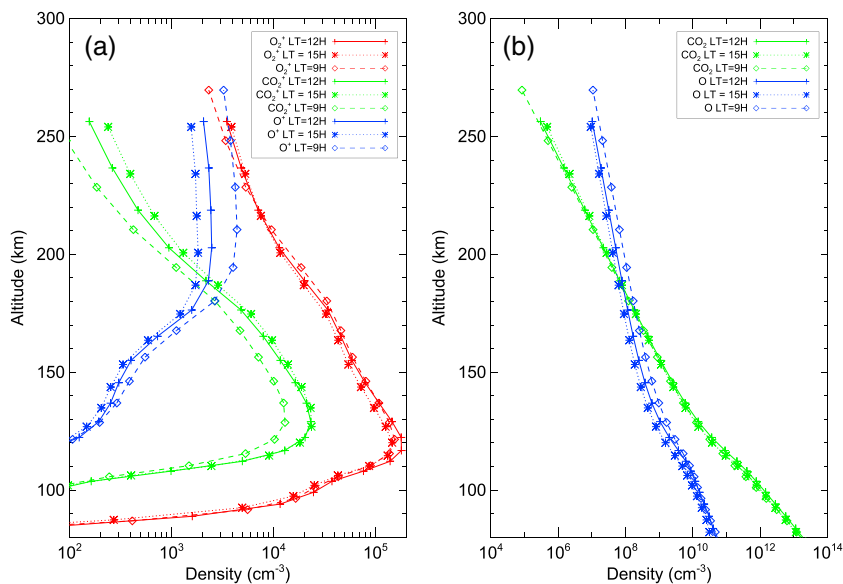


Figure 4. (a) Comparison of the computed density profiles of O₂⁺ (red), O⁺ (blue), and CO₂⁺ (green) at different local times: LT = 12 h (solid lines), LT = 9 h (dashed lines), and LT = 15 h (dotted lines), at the equator at Ls = 0° for solar average conditions. (b) Comparison of the computed CO₂⁺ (green) and O⁺ (blue) density at the same local times.

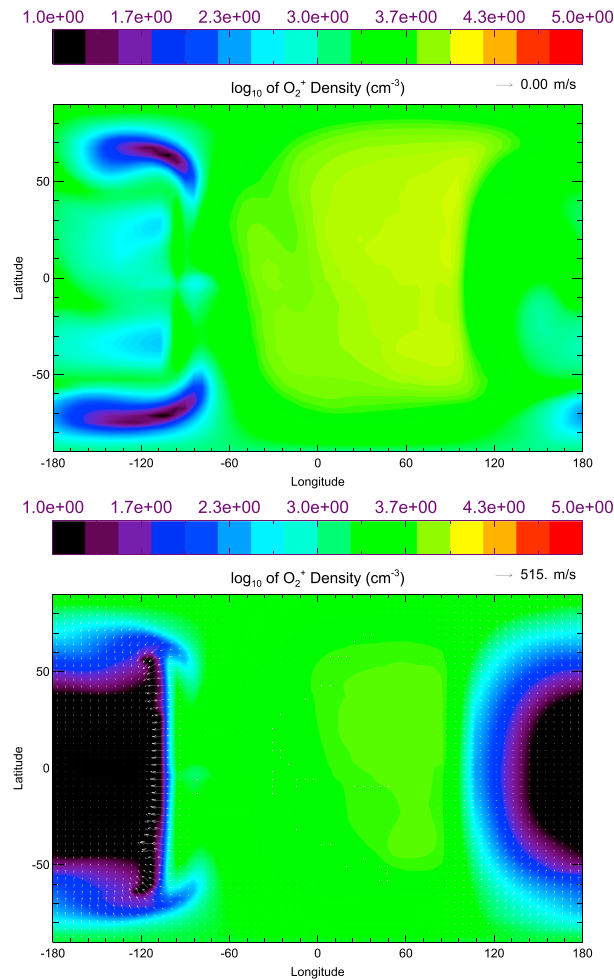


Figure 5. (top) Simulated horizontal map of the O_2^+ density at the pressure level $P = 8 \times 10^{-8}$ Pa (near the exobase ~ 180 – 250 km) at $L_s = 0^\circ$ for solar mean conditions, without the ion dynamics. The density is a \log_{10} scale in cm^{-3} . This map corresponds to a snapshot when noon is at longitude $= 0^\circ$. The dayside is at longitudes between $-90^\circ < \varphi < 90^\circ$, and the nightside at longitudes $\varphi < -90^\circ$ and $\varphi > 90^\circ$. The morning side at longitude $\varphi < 0^\circ$ and evening side at longitudes $\varphi > 0^\circ$. (bottom) Same as Figure 5 (top) but with the inclusion of the ion dynamics. The horizontal velocity vectors are represented by the arrows with a linear relation between the size of the arrow and the magnitude of the horizontal velocity. The largest velocity is indicated at the top right of the panel.

densities of O_2^+ and CO_2^+ are only slightly affected by transport. The decrease of the density at the upper level is probably balanced by an upward flux resulting from the very large density gradient between 180 and 250 km. The shape of the O_2^+ and CO_2^+ density profile is in good agreement with Krasnopolsky and Fox models as well, especially the inflection point of the O_2^+ and CO_2^+ density profile that is observed only when dynamics is included. Below 160 km, transport is negligible on the dayside.

The assumption of diffusive equilibrium at the upper boundary is very uncertain. Fox [1997] has shown that changing the vertical velocity can modify the density vertical profiles above 180 km and was able to derive a limiting flux or upper limit of the flux at the upper boundary above which no equilibrium profiles could be simulated. She also finds a good agreement with Viking observations when the flux was fixed to the limiting flux. Here we do not try to derive the limiting flux; we only compare the vertical density profile obtained with a zero vertical velocity and with a vertical velocity equal to + 200 m/s at the upper boundary ($P \sim 2 \times 10^{-8}$ Pa).

electrons at the beginning of the simulation. Typical ion vertical density profiles presented in the next sections are obtained after ~ 4 h.

3. Comparison With Other Models and Observations

The LMD-MGCM electron density at the peak and the altitude of the main peak were compared to numerous MGS and MARSIS/Mars Express observations in a previous study by González-Galindo *et al.* [2013]. Unfortunately, no vertical distribution of the ion composition has been retrieved since Viking observations, so only electron density profiles were used for those comparisons by González-Galindo *et al.* [2013]. The model reproduces the SZA variability of the electron density and the altitude of the peak, although it underestimates the density at the peak by about 20%.

3.1. Comparison With Previous Models

The density profiles obtained with and without ion dynamics at $L_s = 0^\circ$ and solar average conditions at $SZA = 0^\circ$ are displayed in Figure 1. The shape of the density profiles of each ion is in good agreement with 1-D models [Shinagawa and Cravens, 1989; Krasnopolsky, 2002; Fox, 2003; Mendillo *et al.*, 2011]. The transport strongly affects the ionosphere above ~ 180 km ($\sim 10^{-6}$ Pa) especially for O^+ , N^+ , and C^+ ions. The O^+ density profile at photoequilibrium is very different from the diffusive equilibrium profile and presents a large upward density gradient, which leads to a strong downward flux. Therefore, the peak density moves downward. Similar profiles are obtained for other minor species C^+ and N^+ . The

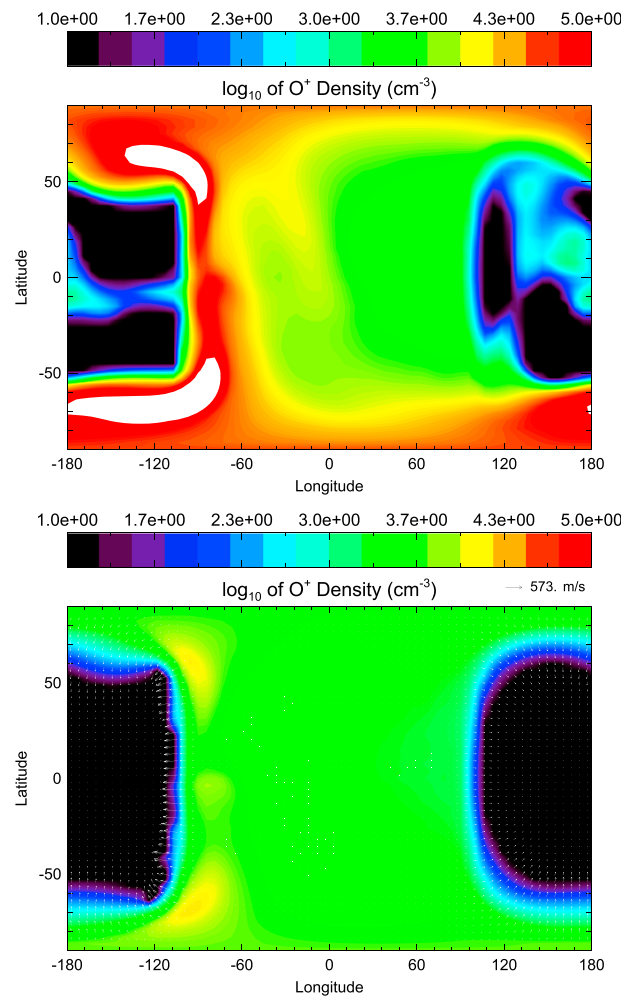


Figure 6. Same as Figure 5 for O⁺ density.

This latter assumption leads to a flux lower than the limiting flux computed by Fox [1997] or the one used by Krasnopolsky [2002] (300 m/s) to simulate the flow to nightside. The comparison of the vertical density profiles obtained with a vertical velocity at the upper boundary equal to 0 m/s and 200 m/s is displayed in Figure 2. The general trends are in good agreement with the results of Fox [1997]. Adding a loss process at the top (positive vertical velocity at top) empties the upper ionosphere and so reduces the density of all ions above 180 km. CO₂⁺ density is less modified. O⁺ is mainly produced at high altitude and can be lost more easily. O⁺ and O₂⁺ densities are reduced by a factor of ~2 at the top boundary when we add an escape process with an effusion velocity of 200 m/s.

Given that this upper boundary has been interpreted not as an escape flow but as diurnal flow in 1-D models, there is no reason to include it in our 3-D model in which diurnal flow is simulated. Therefore, in all the next sections, we will assume no vertical flux at the top boundary. O₂⁺ and CO₂⁺ densities obtained on the dayside outside the crustal field regions from Najib *et al.* [2011] are in rather good agreement (within a factor of 2 between 200 and 250 km) with our results. Differences in the magnitude of ion densities are most likely

due to differences in the neutral atmospheric density, which is an input in Ma *et al.* [2004] and self-consistently calculated in our model. We think that comparing the effects of different processes is more interesting than simply comparing density profiles, since such a comparison will be shifted to discuss differences in the neutral atmosphere. The O⁺ density profile on the dayside is different than in Najib *et al.* [2011] but this difference could be explained by the horizontal magnetic field (included in Najib *et al.* [2011] but not in our simulations) that reduces the downward flux [Shinagawa and Cravens, 1989].

Ma *et al.* [2004] show ion density profiles above the crustal field region (see their Figure 6). Crustal field increases the upward transport above ~350 km, but the ion density profiles do not differ significantly from density profiles outside crustal field regions below 350 km in the altitude range of our simulation.

3.2. Comparison With Viking 1 Observations

The comparison with Viking 1 retarding potential analyzer (RPA) observations (Figure 3), obtained at Ls = 97°, shows a reasonable agreement between the observed and the modeled O₂⁺ density profile. The CO₂⁺ density is overestimated by the model by a factor of 2 and the O⁺ density is slightly underestimated. The O⁺ density peak is found at a lower altitude than the observed peak consistent with the model results of Krasnopolsky [2002]. An explanation of the difference suggested by Shinagawa and Cravens [1989] is that horizontal ionospheric magnetic field could prevent downward transport of O⁺ ions. The O⁺ density vertical profile obtained slightly later (Ls = 118°) by Viking 2 is more dispersive but consistent with observations by Viking 1.

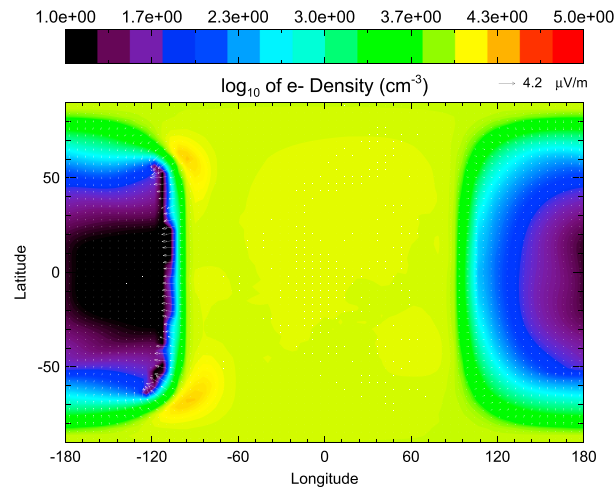


Figure 7. Simulated horizontal map of the electron density at the pressure level $P \sim 8 \times 10^{-8}$ Pa (near the exobase ~ 180 – 250 km) at $L_s = 0^\circ$ for solar mean conditions. The density is a \log_{10} scale in cm^{-3} . This map corresponds to a snapshot when noon is at longitude $= 0^\circ$. The dayside is at longitudes between $-90^\circ < \varphi < 90^\circ$, and the nightside is at longitudes $\varphi < -90^\circ$ and $\varphi > 90^\circ$. Morning side at longitude $\varphi < 0^\circ$ and evening side at longitude $\varphi > 0^\circ$. The horizontal electric field vector is represented by the arrows with a linear relation between the size of the arrow and the magnitude of the horizontal electric field. The largest electric field strength is indicated at top right of the panel.

The difference with the Viking observed O^+ and CO_2^+ densities could be due to the neutral oxygen density that, in our model, is not tuned to obtain a fit to the observations but computed. In pressure coordinates, the O_2^+ density peak is found at the same vertical level as the observed O_2^+ density peak. However, when translated to altitude coordinates, there is a slight difference in the altitude of the O_2^+ density peak ~ 110 – 115 km in our simulations and ~ 130 km from Viking 1 profile. This difference suggests a different thermal structure in the lower atmosphere, although the temperature above 10^{-4} Pa is in good agreement with the neutral temperature derived by Viking 1 mass neutral spectrometer below 160 km ($\sim 10^{-6}$ Pa) [Nier and McElroy, 1977], and slightly lower than the neutral temperature used by Hanson et al. [1977] to fit Viking 1 density profiles from RPA (~ 130 – 140 K) below the ionospheric peak. The average value of the altitude of the peak density observed from Mars Express radar sounding at $L_s = 90^\circ$ is

found near 115 km [Morgan et al., 2008] in better agreement with our model than Viking observations.

In order to compute the pressure coordinate, we extrapolate the temperature by assuming a constant temperature above 160 km (Figure 3b). In Figure 3b, we also display the ion and electron temperature used in our simulations. Unfortunately, no vertical profiles of the ion composition have been retrieved since Viking observations. Future systematic observations by MAVEN Natural Gas and Ion Mass Spectrometer should provide better constrains to understand the role of the transport processes in the Martian upper ionosphere.

4. Spatial and Diurnal Variations

4.1. Vertical Variations

The vertical density profiles obtained at different local times $LT = 9$ h, 12 h, and 15 h for O_2^+ , O^+ , and CO_2^+ , at $L_s = 0^\circ$ and Latitude $= 0^\circ$ and for average solar activity are displayed in Figure 4a. CO_2^+ and O^+ densities at the same local times are displayed in Figure 4b.

O^+ density presents strong variations with local time. A strong dawn/dusk contrast is observed which is linked to a similar asymmetry in the neutral atmosphere at this season [Gonzalez-Galindo et al., 2009a; Vaillie et al., 2009a; Yagi et al., 2012]. At $LT = 9$ h, O^+ becomes the dominant ion above 250 km while at $LT = 15$ h, O_2^+ is the dominant ion at all the simulated altitudes. This local time variation is due to the atomic oxygen density asymmetry (Figure 4b). The O^+ density is larger at $LT = 9$ h than $LT = 15$ h. Atomic oxygen becomes the dominant species at 170 km at $LT = 9$ h and at 190 km at $LT = 15$ h. The CO_2^+ density presents opposite variations with local time due to a more efficient loss process when O^+ density is larger.

4.2. Horizontal Variations

Snapshots of the O_2^+ , O^+ densities at a Martian half rotation, at pressure level $P = 8 \times 10^{-8}$ Pa (~ 180 – 250 km), close to the exobase, with and without the ionosphere dynamics are presented in Figures 5 and 6, respectively.

The main plasma flow is directed from dayside to nightside and the conversion of thermal energy into kinetic energy leads to velocities of few hundred of m/s in the atmospheric frame at the terminator. The value of the

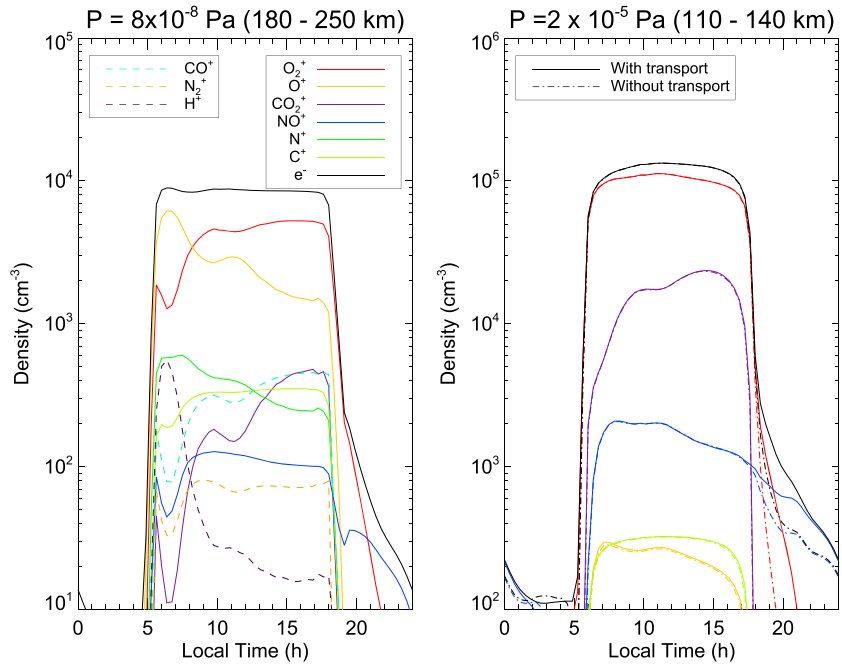


Figure 8. (left) Density of several ions included in the simulation function of the local time at $P = 8 \times 10^{-8}$ Pa (near the exobase $\sim 180\text{--}250$ km). The altitude variations of the pressure level along local time are indicated. Solid lines represent the density of ions for which the dynamical equations are solved. Dashed lines represent the density of ions transported by the neutral winds only. (right) Density of several ions included in the simulation function of the local time at $P = 2 \times 10^{-5}$ Pa. The altitude range of the pressure level along local time is indicated. Solid lines correspond to simulated densities including ion transport. Dashed lines correspond to the simulated density transported by the neutral wind only.

horizontal velocity could be sensitive to uncertainties in some parameters used in the model. These possible small systematic biases in the model do not invalidate the results of the main variations presented here (seasonal, local time, and solar cycle).

The horizontal gradients are larger at dawn than duskside because of the planetary rotation. Supersonic transterminator flow has been derived from ASPERA-3 IMA measurements between 290 and 500 km altitude,

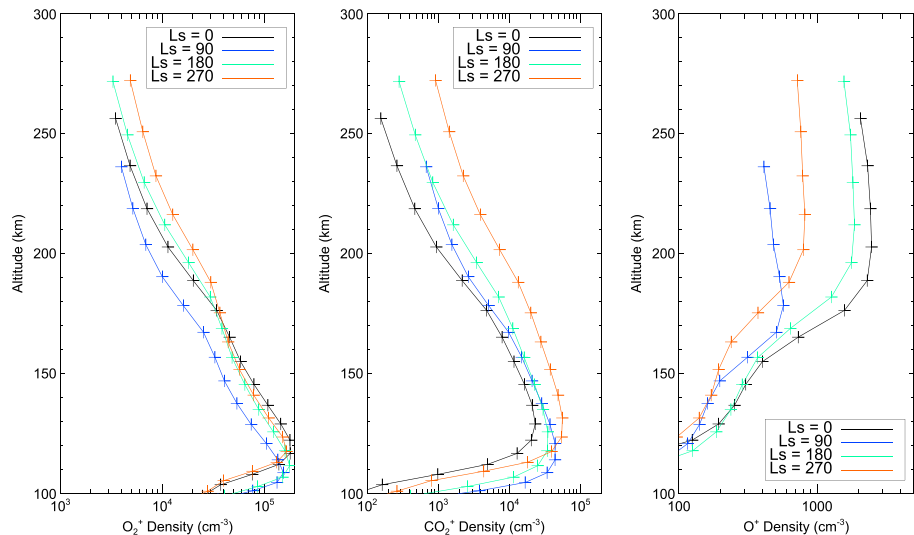


Figure 9. Vertical density profiles of (left) O_2^+ , (middle) O^+ , and (right) CO_2^+ above the subsolar point, for solar average conditions, at different solar longitudes.

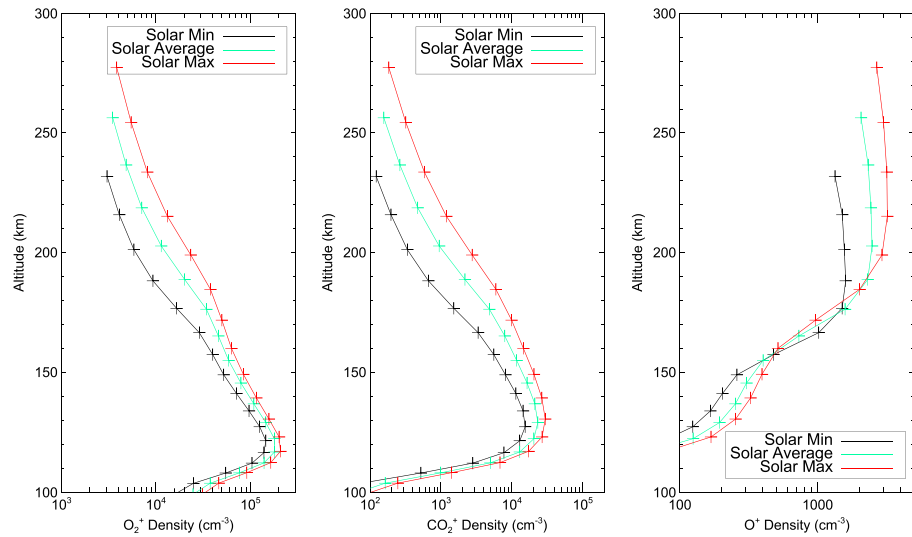


Figure 10. Vertical density profiles of (left) O_2^+ , (middle) O^+ , and (right) CO_2^+ above the subsolar point, at $L_s = 0^\circ$, for different solar activities.

attributed to ionospheric pressure gradient from dayside to nightside or to momentum transfer from the solar wind [Fränzl et al., 2010]. We obtain a transterminator velocity between 0.5 and 1 km/s at higher altitudes ~ 250 km due to the dayside/nightside pressure gradient that is only a small fraction (20%) of the velocity measured by ASPERA-3 IMA. We believe that the transterminator velocity could be mainly driven by the solar wind and therefore could be the main cause of difference between the model and observed velocities. It is also possible that the exponential increase of the transterminator velocity with altitude (see section 5) leads to much larger transterminator velocity at 500 km than the computed velocity at 250 km, corresponding to the upper altitude of the ASPERA-3 IMA measurements. Large vertical increases of the transterminator flow have also been simulated in the Venusian upper ionosphere from 100 to 600 km by Elphic et al. [1984].

The spatial variations of O_2^+ and O^+ densities near the exobase are more complex than a simple decrease with SZA. The same global spatial relative structure is observed on the dayside whether or not dynamics are included, showing that horizontal movements affects only slightly the ionospheric daytime density latitude-local time

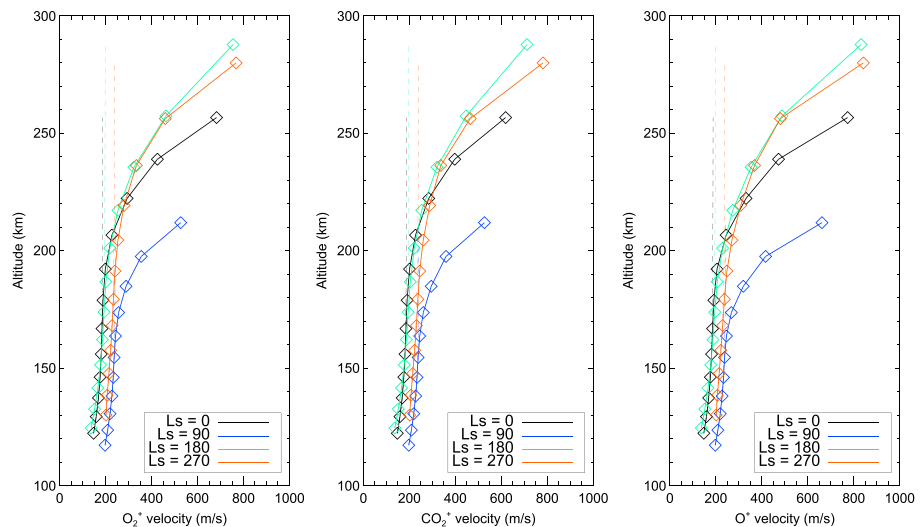


Figure 11. Vertical profile of the horizontal velocity, averaged along the terminator of (left) O_2^+ , (middle) O^+ , and (right) CO_2^+ , at one time step (middle time of the simulation) for solar average conditions, at different solar longitudes. The horizontal neutral wind velocity is indicated by dashed lines.

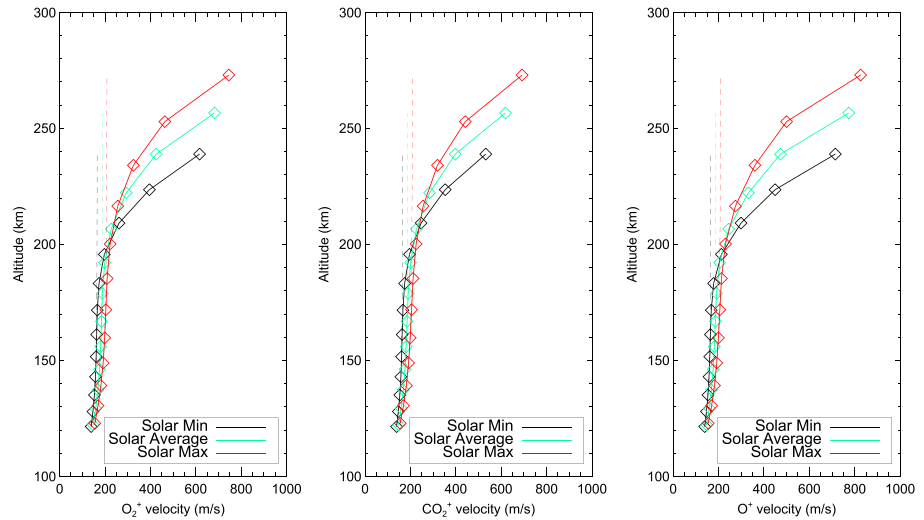


Figure 12. Vertical profile of the horizontal velocity, averaged along the terminator of (left) O_2^+ , (middle) O^+ , and (right) CO_2^+ at one time step (middle time of the simulation) at $L_s = 0^\circ$, for different solar activities. The horizontal neutral wind velocity is indicated by dashed lines.

structure. The dawn/dusk asymmetry of the O^+ density, noted in section 4.1, is observed along with a smoother horizontal density gradient at the evening side than at the morning side. As a consequence of the steeper gradient at the morning side, stronger ionospheric winds (~300–500 m/s) are observed on this side. It is interesting to note that such an asymmetry in the ion flow pattern at Venus (but in the Venusian case with a stronger flow at evening side than morning side) was also observed by PVO retarding potential analyzer (ORPA) experiment [Miller and Whitten, 1991] but its cause was not established. The stronger dusk atmospheric flow simulated by Venus Thermosphere Global Circulation Model (VTGCM) [Bougher et al., 1999], compared to dawn atmospheric flow, could reduce the dusk horizontal ion pressure gradient leading to an asymmetry between morning side and evening side.

Observations by ORPA on PVO have provided much information on the ionospheric dynamics of Venus. A comparison between Venus and Mars is appropriate because of the lack of internal magnetic field, even if the difference between rotation and flow patterns of Mars and Venus are to be considered [Bougher et al., 1999]. Because of the lack of internal magnetic field, the ionosphere is very sensitive to pressure gradients for both planets. The velocity variations obtained in our model show the same three regions (dayside, terminator, and nightside) observed by Miller and Whitten [1991], but the nightside flow is not chaotic.

When plasma dynamics are not included in the model, the chemical lifetime of the O_2^+ ions at altitudes close to the exobase is large due to the low atmospheric and electron densities. As the vertical component of the neutral wind is low, the ions can be transported to the nightside efficiently, with a slight decrease of

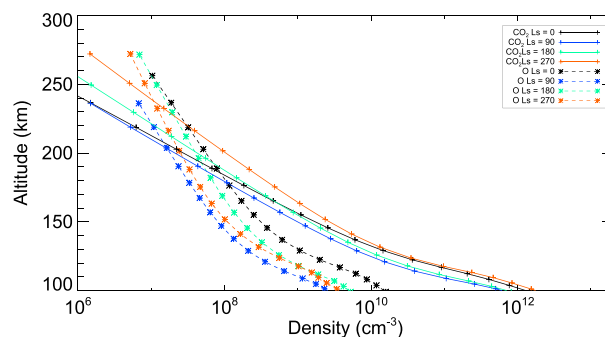


Figure 13. Vertical density profiles of (left) O^+ and (right) CO_2^+ above subsolar point, for solar average conditions, at different solar longitudes.

the density from dusk to dawn due to chemical loss. When the plasma dynamics is included, the nightside O_2^+ ions are transported downward to altitudes where their lifetime is shorter and can be efficiently lost by chemical reactions. The O_2^+ density between 120 and 150 km on the nightside is slightly larger when plasma dynamics is included. A similar behavior is observed for NO^+ ions. The chemical lifetimes of O^+ and CO_2^+ are shorter than that for O_2^+ , and therefore, their densities are low on the nightside with and without dynamics.

Table 1. O_2^+/O^+ and CO_2^+/O^+ Dayside Average Density Ratios at $P = 8 \times 10^{-8}$ Pa (Near the Exobase) for Northern Spring ($L_s = 0^\circ$), Northern Summer ($L_s = 90^\circ$), Northern Autumn ($L_s = 180^\circ$), and Northern Winter ($L_s = 270^\circ$)

Density Ratios at $P = 8 \times 10^{-8}$ Pa	$L_s = 0^\circ$	$L_s = 90^\circ$	$L_s = 180^\circ$	$L_s = 270^\circ$
O_2^+/O^+	1.2	10.6	1.8	8.1
CO_2^+/O^+	0.06	2.0	0.17	1.8

The electron density and horizontal electric field are displayed in Figure 7. On the dayside, the electron density is roughly equal to the sum of O_2^+ and O^+ density, while the electron density is very low near the exobase on the nightside, in agreement with MaRS observations [Withers et al., 2012b], but in contrast with the Venusian ionosphere [Brace and Kliore, 1991]. The strongest horizontal electric field values are found at the terminator, morning side with typical values of 3–4 $\mu\text{V/m}$ at $P = 8 \times 10^{-8}$ Pa. Typical values of the electric field produced by convection ($-\mathbf{v}_e \times \mathbf{B}$) would be $\sim w_e B \sim 5 \mu\text{V}$ assuming $w_e = 100$ m/s and $B = 50$ nT, and therefore, the same order of magnitude as the electron pressure gradient term (equation (3a)). Therefore, at the terminator, the horizontal electric field could at most be increased by a factor of 2 when including the magnetic field.

The local time variations of the densities of all ions and electrons at the equator at $P \sim 2 \times 10^{-5}$ Pa and $P \sim 8 \times 10^{-8}$ Pa are displayed in Figure 8. At $P = 2 \times 10^{-5}$ Pa, the results obtained without the ion dynamics are also displayed to show the importance of the nightside downward flux on the O_2^+ and NO^+ density at duskside. At $P = 8 \times 10^{-8}$ Pa, the strong density increase at dawn is observed not only for O^+ but also for N^+ and H^+ ions (H^+ is only transported by the neutral wind in these simulations). According to our simulations,

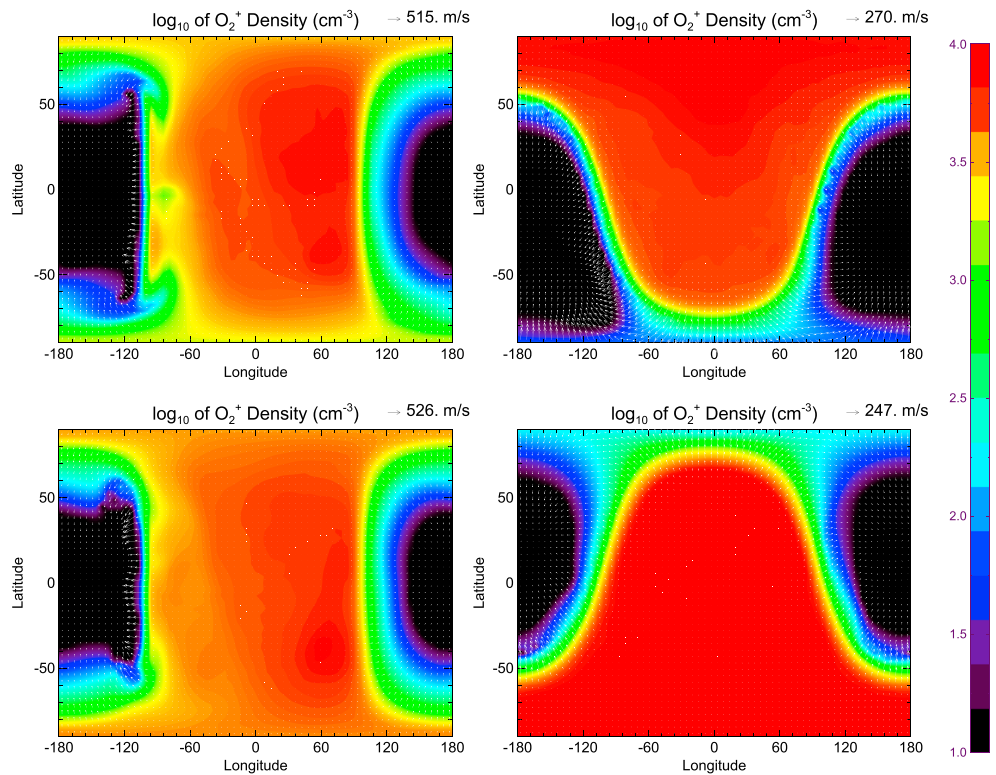


Figure 14. Simulated horizontal maps of the O_2^+ density at the pressure level $P = 8 \times 10^{-8}$ Pa (near the exobase) at (top left) $L_s = 0^\circ$, (top right) $L_s = 90^\circ$, (bottom left) $L_s = 180^\circ$, and (bottom right) $L_s = 270^\circ$ for solar average conditions. The density is a \log_{10} scale in cm^{-3} . These maps correspond to snapshots when noon is at longitude $= 0^\circ$. The dayside is at longitudes between $-90^\circ < \varphi < 90^\circ$, and the nightside is at longitudes $\varphi < -90^\circ$ and $\varphi > 90^\circ$. Morning side at longitude $\varphi < 0^\circ$ and evening side at longitudes $\varphi > 0^\circ$. The horizontal velocity vectors are represented by the arrows with a linear relation between the size of the arrow and the magnitude of the horizontal velocity. The largest velocity is indicated at the top right of the panel.

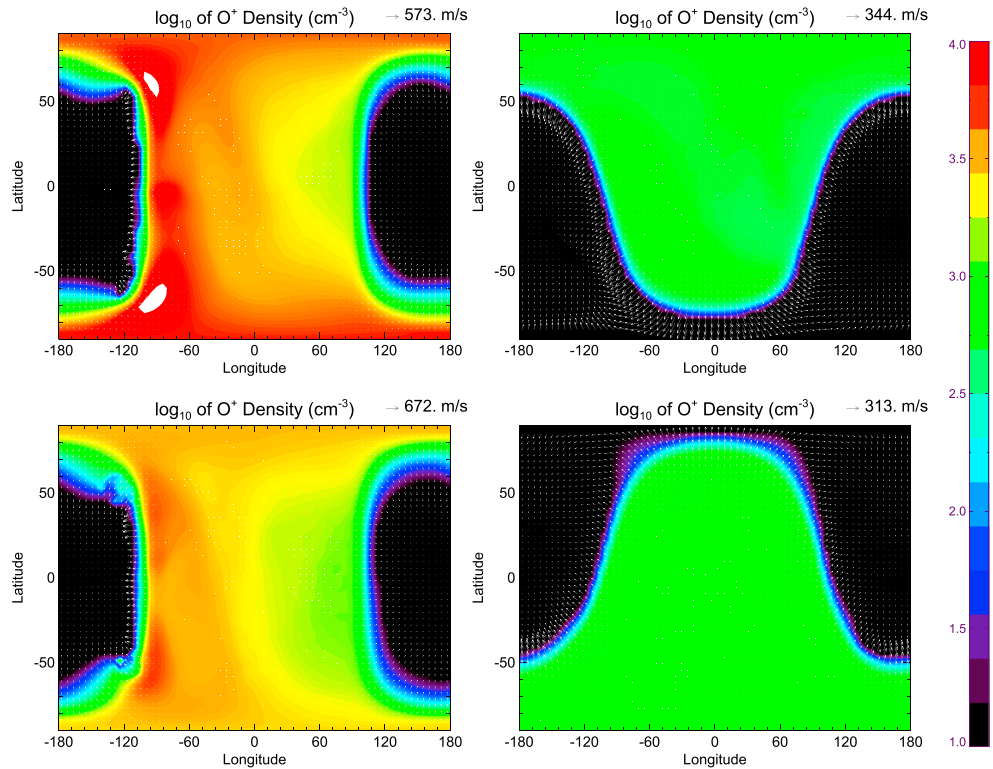


Figure 15. Same as Figure 14 for O^+ density.

O^+ becomes the dominant ion at the exobase on the morning side ($6 \text{ h} < \text{LT} < 8 \text{ h}$). O_2^+ and NO^+ are not chemically destroyed immediately on the nightside because of their large photochemical lifetimes. There is a slow decrease of the NO^+ density from evening to morning sides (see *González-Galindo et al. [2013]* for a more detailed study).

We also address the effects of the ions on the neutral atmosphere (friction and heating). A comparison between simulations done with and without this retroaction does not show any differences in the neutral atmospheric velocity and temperature. The coupling between neutrals and ions is stronger at low altitudes ($< 200 \text{ km}$) where ion velocities and temperatures are close to the neutral ones. When the ion and electron velocities and temperatures differ from neutrals above 200 km , the coupling is too weak to be efficient.

5. Seasonal and Solar Activity Variations

To study the seasonal variations of the ionosphere and its variations with the solar activity, we perform simulations of one Martian rotation at $L_s = 0^\circ$ (northern spring), $L_s = 90^\circ$ (northern summer), $L_s = 180^\circ$ (northern autumn), and $L_s = 270^\circ$ (northern winter) for three different solar activities: low solar activity, average solar activity, and high solar activity, as described in *González-Galindo et al. [2005]*.

The vertical profiles of O_2^+ , O^+ , and CO_2^+ ions, at the subsolar point, for the four seasons at solar average conditions are displayed in Figure 9; the profiles above subsolar point at $L_s = 0^\circ$ for low, average, and high solar activities are displayed in Figure 10. Similar plots for the vertical profile of the horizontal velocity components are displayed in Figures 11 and 12. The neutral profiles of O^+ and CO_2^+ above the subsolar point for each season are displayed in Figure 13 for average solar conditions only.

The seasonal variation of the O_2^+ densities peak layer results from the inflation/contraction of the atmosphere driven by seasonal variations of the temperatures in the lower atmosphere [see *González-Galindo et al., 2013*]. There is a strong seasonal variation, to a first order in opposite direction, in the O^+ and CO_2^+ density profiles (Figure 9). The seasonal variations are due to the larger O^+ density in the Martian thermosphere at equinoxes than at solstices at high altitudes (Figure 13). As shown in section 3, the O^+

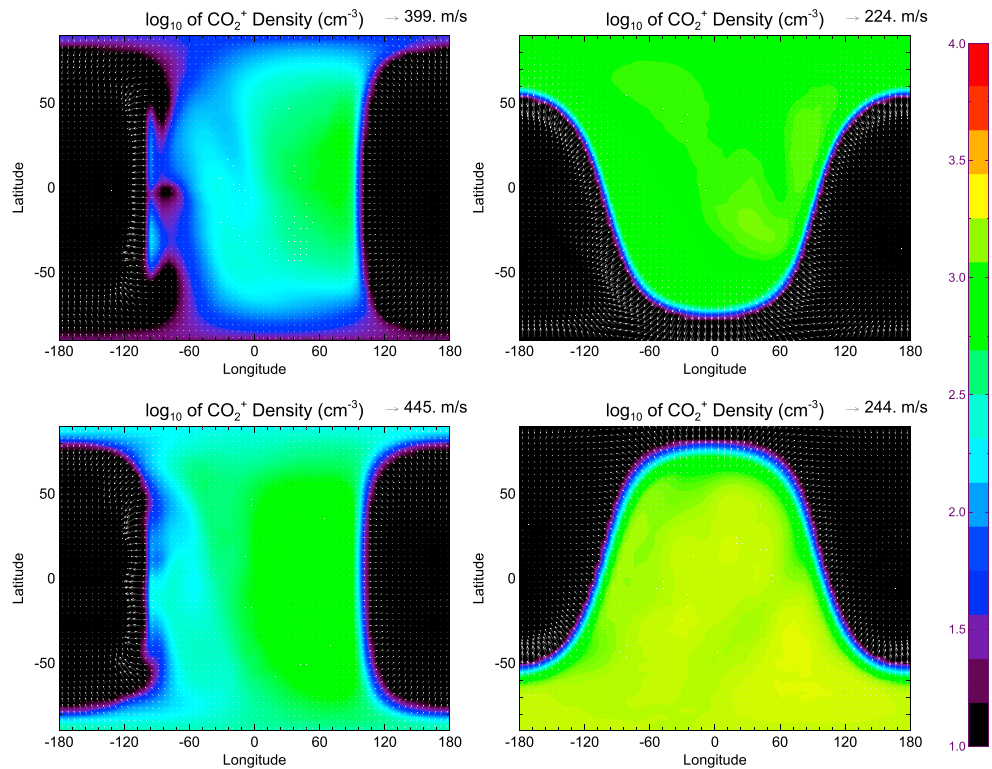


Figure 16. Same as Figure 14 for CO_2^+ density.

density above 160 km is controlled by the downward flux from higher altitudes (>200 km), when the diffusive equilibrium is used at the top of the atmosphere, and therefore large O^+ density above 200 km provides a larger source of O^+ ion by photoionization. O^+ can react with CO_2^+ to form O_2^+ [Stewart et al., 1972]. This reaction is important at lower altitudes where the CO_2^+ density is largest. These seasonal variations of ionospheric composition should be observed in the composition of the escape flux as measured by the energetic particles detector ASPERA-3 on Mars Express [Barabash et al., 2007; Carlsson et al., 2006]. The average dayside ratios of the density of CO_2^+/O^+ and O_2^+/O^+ at $P=8 \times 10^{-8}$ Pa at each season are given in Table 1, showing variations of 1 order of magnitude in the relative composition on the dayside upper ionosphere.

The larger O^+ density at equinoxes is due to the homopause position at lower altitudes [Gonzalez-Galindo et al., 2009a]. This lower altitude of the homopause enhances the vertical transport of light species such as O and H (Chaufray et al., submitted to Icarus, 2012). This seasonal variation of the homopause altitude was interpreted by Gonzalez-Galindo et al. [2009a] as a more intense mixing owing to a reinforced circulation during solstices, which can be noted in Figures 11 and 12 by the larger horizontal component of the atmospheric velocity. The magnitude of the horizontal velocity of the different ions, at the terminator, increases exponentially with the altitude due to the decrease of the friction with neutrals at high altitudes. The seasonal variations and the variations due to the solar activity of the ion dynamics (Figures 11 and 12) are mainly due to the expansion of the Martian atmosphere resulting from the heating by solar UV flux. There is a slight increase of the horizontal plasma velocity with solar activity of 10% from low solar activity to average solar activity and of 20% from low solar activity to high solar activity at the exobase. These percentages are similar to the percentages of the atmospheric horizontal velocity. Similar increases of the dynamics with the EUV flux was observed by Valeille et al. [2009b] in their 3-D simulations of the neutral thermosphere.

Horizontal velocities of the different ions are very close to each other, making the single-fluid approximation a reasonable assumption for the ionospheric plasma. As physically expected, the densities of all ions increase with the solar activity.

Maps of the O_2^+ , CO_2^+ , and O^+ densities at $P = 8 \times 10^{-8}$ Pa for all seasons are displayed in Figures 14–16.

The main seasonal effect is due to the Martian axial tilt which moves the subsolar point northward during northern summer solstice and southward during northern winter solstice. The largest horizontal velocities are observed at the terminator for all seasons. The seasonal variations and the anticorrelation of the O^+ and CO_2^+ density are observed at all latitudes and local times. Morphology of the maps is not modified significantly in our model by the solar activity (not shown). Solar activity changes mainly the neutral temperature, and therefore, the vertical extension of the ionosphere as well as the ion densities.

6. Conclusion

We have developed a 3-D dynamical model of the Martian ionosphere within the LMD Martian general circulation model. This model is used to simulate the coupled variations of the ionosphere-thermosphere until the exobase. On the dayside, ion dynamics are important above ~ 180 km, especially for ions produced at high altitudes such as O^+ . On the nightside, ions produced at high altitudes are transported downward due to pressure gradients and help to maintain a tenuous nightside ionosphere of Mars in the lower thermosphere. Seasonal and diurnal variations of the ionospheric composition are observed at the exobase resulting from the dynamics of the neutral atmosphere. These seasonal variations could lead to similar variations of the composition of the escaping plasma. Several improvements will be added in the future to study the effects of the crustal and ionospheric magnetic fields as well as computing the heating and cooling processes of the Martian ionosphere in order to better understand their effects on the Martian upper ionosphere. The MAVEN observations should provide numerous new observations dedicated to the study of the Martian upper atmosphere and ionosphere and their roles in the escape processes that will be analyzed with our model.

Appendix A: Horizontal Dynamics Solver

A description of the numerical grid and the fundamental dynamical equations solved for the neutral atmosphere is based on *Sadourny* [1975], *Sadourny and Laval* [1984], and discussed in *Hourdin* [2005] and technical notes from *Hourdin* [2010]. The numerical scheme used to solve the horizontal dynamics of the ionospheric plasma is based on the neutral dynamics numerical scheme. In this appendix we detailed the horizontal dynamics equations rewritten in the model's coordinates.

A1. Numerical Spatial Grids

The horizontal dynamics equation corresponding to the meridional and zonal dynamics is solved using X - Y horizontal grids linked to longitude λ and latitude θ by the bijective relations (A1a) and (A1b)

$$X = 1 + \frac{l}{2} \left(1 + \frac{\lambda}{\pi} \right), \quad \lambda \in [-\pi, \pi], \quad X \in [1, l + 1] \quad (A1a)$$

$$Y = 1 - \frac{J(\sin\theta - 1)}{2}, \quad \theta \in [-\pi/2, \pi/2], \quad Y \in [1, 1 + J] \quad (A1b)$$

where l and J are the number of discretization points minus 1 along the longitude and latitude, respectively. In our simulations, $l = 64$ and $J = 48$.

The zonal and meridional derivatives of any scalar field A are linked to the derivatives in the new coordinates system X and Y by the relations

$$\frac{\partial A}{\partial \lambda} = \left| \frac{dX}{d\lambda} \right| \frac{\partial A}{\partial X} = \frac{1}{\varphi} \frac{\partial A}{\partial X} \quad (A2a)$$

$$\frac{\partial A}{\partial \theta} = \left| \frac{dY}{d\theta} \right| \frac{\partial A}{\partial Y} = \frac{1}{\xi(\theta)} \frac{\partial A}{\partial Y} \quad (A2b)$$

where φ and ξ functions are derived from (A1a) and (A1b). A hybrid η coordinate is used on the vertical grid and defined by two fixed profiles $A(\eta)$ and $B(\eta)$, such as

$$P(X, Y, \eta, t) = A(\eta)P_s(X, Y, t) + B(\eta) \quad (\text{A3})$$

where $P(X, Y, \eta, t)$ is the pressure at (X, Y, η, t) and $P_s(X, Y, t)$ the surface pressure at (X, Y, t) . At ionospheric levels, $A(\eta) \sim 0$ and therefore iso- η surfaces correspond to isobar surfaces.

Under this new vertical variable, the spatial and temporal derivative of a scalar field A are given by relations (A4a)–(A4d)

$$\left(\frac{\partial A}{\partial t}\right)_{X,Y,z} = \left(\frac{\partial A}{\partial t}\right)_{X,Y,\eta} + \left(\frac{\partial A}{\partial \eta}\right)_{X,Y,t} \left(\frac{\partial \eta}{\partial t}\right)_{X,Y,z} \quad (\text{A4a})$$

$$\left(\frac{\partial A}{\partial X}\right)_{Y,z,t} = \left(\frac{\partial A}{\partial X}\right)_{Y,\eta,t} + \left(\frac{\partial A}{\partial \eta}\right)_{X,Y,t} \left(\frac{\partial \eta}{\partial X}\right)_{Y,z,t} \quad (\text{A4b})$$

$$\left(\frac{\partial A}{\partial Y}\right)_{X,z,t} = \left(\frac{\partial A}{\partial Y}\right)_{X,\eta,t} + \left(\frac{\partial A}{\partial \eta}\right)_{X,Y,t} \left(\frac{\partial \eta}{\partial Y}\right)_{X,z,t} \quad (\text{A4c})$$

$$\left(\frac{\partial A}{\partial z}\right)_{X,Y,t} = \left(\frac{\partial A}{\partial \eta}\right)_{X,Y,t} \left(\frac{\partial \eta}{\partial z}\right)_{X,Y,t} \quad (\text{A4d})$$

If A is the gravitational potential $\Phi = gz$, where g is the acceleration due to gravity and z the altitude, we derive the following equations

$$-\left(\frac{\partial \Phi}{\partial X}\right)_{Y,\eta,t} / \left(\frac{\partial \Phi}{\partial \eta}\right)_{X,Y,t} = \left(\frac{\partial \eta}{\partial X}\right)_{Y,z,t} \quad (\text{A5a})$$

$$-\left(\frac{\partial \Phi}{\partial Y}\right)_{X,\eta,t} / \left(\frac{\partial \Phi}{\partial \eta}\right)_{X,Y,t} = \left(\frac{\partial \eta}{\partial Y}\right)_{X,z,t} \quad (\text{A5b})$$

$$1 = \left(\frac{\partial z}{\partial \eta}\right)_{X,Y,t} \left(\frac{\partial \eta}{\partial z}\right)_{X,Y,t} \quad (\text{A5c})$$

Replacing A by the pressure P in equation (A4d) and using the hydrostatic equation $(\partial P / \partial z)_{X,Y,t} = -\rho_N g$, where ρ_N is the atmospheric mass density we find

$$-\rho_N g = \left(\frac{\partial P}{\partial \eta}\right)_{X,Y,t} \left(\frac{\partial \eta}{\partial z}\right)_{X,Y,t} \quad (\text{A6})$$

Using equation (A5c), we derive

$$\left(\frac{\partial P}{\partial \eta}\right)_{X,Y,t} = -\rho_N g \left(\frac{\partial z}{\partial \eta}\right)_{X,Y,t} \quad (\text{A7})$$

Using (A7) and replacing gz by Φ , the hydrostatic equation can be written

$$\left(\frac{\partial P}{\partial \eta}\right)_{X,Y,t} = -\rho_N \left(\frac{\partial \Phi}{\partial \eta}\right)_{X,Y,t} \quad (\text{A8})$$

and finally horizontal spatial derivatives of a field scalar A can be expressed by

$$\left(\frac{\partial A}{\partial X}\right)_{Y,z,t} = \left(\frac{\partial A}{\partial X}\right)_{Y,\eta,t} + \rho_N \left(\frac{\partial A}{\partial P}\right)_{X,Y,t} \left(\frac{\partial \Phi}{\partial X}\right)_{Y,\eta,t} \quad (\text{A9a})$$

$$\left(\frac{\partial A}{\partial Y}\right)_{X,z,t} = \left(\frac{\partial A}{\partial Y}\right)_{X,\eta,t} + \rho_N \left(\frac{\partial A}{\partial P}\right)_{X,Y,t} \left(\frac{\partial \Phi}{\partial Y}\right)_{X,\eta,t} \quad (\text{A9b})$$

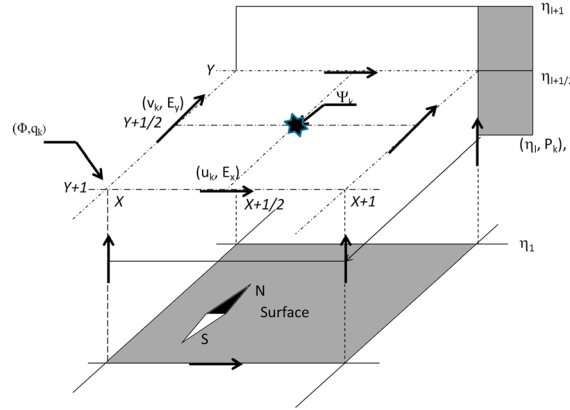


Figure A1. Scheme of the numerical grid positions used to compute the ion mass mixing ratio (q_k), zonal, meridional, and vertical components of the ion velocity (u_k , v_k , and w_k), and electric field components (E_x , E_y , and E_z), adapted from Hourdin 1994. The ion partial pressure P_k , the gravitational potential Φ , the ion vorticity Ψ_k , and the hybrid coordinate η are also indicated. X is the discretization index of the zonal direction, Y the discretization of the meridional direction, and L the discretization of the vertical index. The star indicates the grid point of ion vorticity Ψ_k .

Using the above relations, it is possible to show that Eulerian derivative is formally not changed:

$$\begin{aligned} \left(\frac{DA}{DT}\right) &= \left(\frac{\partial A}{\partial t}\right)_z + u \left(\frac{\partial A}{\partial x}\right)_z + v \left(\frac{\partial A}{\partial y}\right)_z + \frac{dz}{dt} \left(\frac{\partial A}{\partial z}\right) \\ &= \left(\frac{\partial A}{\partial t}\right)_\eta + u \left(\frac{\partial A}{\partial x}\right)_\eta + v \left(\frac{\partial A}{\partial y}\right)_\eta + \frac{d\eta}{dt} \left(\frac{\partial A}{\partial \eta}\right) \end{aligned} \quad (A10)$$

where only index z and η are written for clarity.

Therefore, the continuity equations are not changed as well as the total derivative of velocity in the horizontal dynamics equations (leading to vorticity and volume kinetic energy gradients).

In the horizontal dynamics equations, only the horizontal pressure gradients must be replaced using equations (A9a) and (A9b).

A2. Horizontal Dynamics Equations

Using the above relations, noting $C_u = a \cos \theta \phi(\lambda)$ and $C_v = a \zeta(\theta)$, The zonal and meridional velocity components, given by equation (2a), are solutions of the differential equations.

$$\begin{aligned} \frac{\partial u_k}{\partial t} + w_k \frac{\partial u_k}{\partial z} - (\zeta_k + 2\Omega \sin \theta) v_k + \frac{1}{C_u} \frac{\partial}{\partial X} \left(\frac{u_k^2 + v_k^2}{2} \right) &= -v_{kn} (u_k - u_n) - \frac{1}{\rho_k} \frac{1}{C_u} \left(\frac{\partial P_k}{\partial X} + \rho_N \frac{\partial \Phi}{\partial X} \right) + \frac{Z_k e}{m_k} E_X \\ \frac{\partial v_k}{\partial t} + w_k \frac{\partial v_k}{\partial z} + (\zeta_k + 2\Omega \sin \theta) u_k + \frac{1}{C_v} \frac{\partial}{\partial Y} \left(\frac{u_k^2 + v_k^2}{2} \right) &= -v_{kn} (v_k - v_n) - \frac{1}{\rho_k} \frac{1}{C_v} \left(\frac{\partial P_k}{\partial Y} + \rho_N \frac{\partial \Phi}{\partial Y} \right) + \frac{Z_k e}{m_k} E_Y \end{aligned}$$

We define the covariant zonal and meridional velocity and electric field components by $\tilde{u} = C_u \times u$, $\tilde{v} = C_v \times v$, $\tilde{E}_X = C_u \times E_X$, $\tilde{E}_Y = C_v \times E_Y$, and the contravariant zonal and meridional velocity by $\tilde{U} = u/C_u$ and $\tilde{V} = v/C_v$ and noting $\Psi_k = (\zeta_k + 2\Omega \sin \theta) C_u C_v$.

We finally have to solve the equations

$$\begin{aligned} \frac{\partial \tilde{u}_k}{\partial t} + w_k \frac{\partial \tilde{u}_k}{\partial z} - \Psi_k \tilde{v}_k + \frac{\partial}{\partial X} \left(\frac{u_k^2 + v_k^2}{2} \right) &= -v_{kn} (\tilde{u}_k - \tilde{u}_n) - \frac{1}{\rho_k} \left(\frac{\partial P_k}{\partial X} + \rho_N \frac{\partial \Phi}{\partial X} \right) + \frac{Z_k e}{m_k} \tilde{E}_X \\ \frac{\partial \tilde{v}_k}{\partial t} + w_k \frac{\partial \tilde{v}_k}{\partial z} + \Psi_k \tilde{u}_k + \frac{\partial}{\partial Y} \left(\frac{u_k^2 + v_k^2}{2} \right) &= -v_{kn} (\tilde{v}_k - \tilde{v}_n) - \frac{1}{\rho_k} \left(\frac{\partial P_k}{\partial Y} + \rho_N \frac{\partial \Phi}{\partial Y} \right) + \frac{Z_k e}{m_k} \tilde{E}_Y \end{aligned}$$

The horizontal components of velocity and vorticity are defined on shifted grids (Figure A1). Zonal equation is solved on the zonal velocity grid and meridional equation is solved on the meridional velocity grid. All other parameters are interpolated linearly.

The horizontal components of the electric field are derived from the electron motion equations (equations (3a) and (3b)) rewritten in hybrid coordinates.

A3. Continuity Equations

We split the continuity equation between neutral advection and plasma dynamics advection in the neutral frame (equations (2a) and (2b)). The advection by the neutral atmosphere is not changed compared to previous models [Forget et al., 1999]. To compute the plasma advection in neutral frame, we use the same algorithm as

for atmospheric advection developed by Hourdin and Armengaud [1998]. This scheme is conservative, positive, and monotonic. It is based on a finite-volume scheme proposed by Van Leer [1977], in which the mass flux of each species crossing the volume boundaries is the product of the total mass flux at the boundary multiplied by an estimate of the subgrid-scale mass mixing ratio of the species derived from a linear interpolation with a slope limitation. The computation of the subgrid-scale mixing ratio requires the knowledge of the neutral mass flux crossing the boundaries [from Hourdin and Armengaud, 1998, equations (12) and (13)]. Using the notation of Hourdin and Armengaud [1998], $U_{X-1/2}$ and $U_{X+1/2}$ fluxes are the atmospheric mass flux that would cross the considered volume at the interface $X-1/2$ and $X+1/2$ if the neutral atmosphere moved by an additional $u_k - u_n$ velocity, where u_k is the velocity of the ion k and u_n the neutral velocity. The total atmospheric mass m^* in the considered volume after the movement is unchanged and equal to the total atmospheric mass m in the same volume before the movement, because the total ion mass represents a negligible part of the total atmospheric mass at all altitudes. With these changes, the algorithm by Hourdin and Armengaud [1998] used to compute the advection by the neutral atmosphere can be used straightforwardly without any further changes. Only horizontal advection is computed using this scheme because vertical plasma advection in the neutral atmospheric frame is computed through the diffusion equation (equation (9)).

Acknowledgments

This work was funded by HELIOSARES project supported by the ANR (ANR-09-BLAN-0223). We would like to thank E. Millour for his help in the GCM installation and compilation with the new ionospheric dynamical core. F.G.G. is funded by a CSIC JAE_Doc contract cofinanced by the European Social Fund. F.G.G. and M.A.L.V. thank the Spanish MICINN for funding support through the CONSOLIDER program "ASTROMOL" CSD2009-00038 and through project AYA2011-23552/ESP. In addition, we thank two anonymous reviewers for their constructive comments and corrections that improved this manuscript.

References

- Angelats i Coll, M., F. Forget, M. A. López-Valverde, P. L. Read, and S. R. Lewis (2004), Upper atmosphere of Mars up to 120 km: Mars Global Surveyor accelerometer data analysis with the LMD general circulation model, *J. Geophys. Res.*, *109*, E01011, doi:10.1029/2003JE002163.
- Angelats i Coll, M., F. Forget, M. A. Lopez-Valverde, and F. Gonzalez-Galindo (2005), The first Mars thermospheric general circulation model: The Martian atmosphere from the ground to 240 km, *Geophys. Res. Lett.*, *32*, 4201, doi:10.1029/2004GL021368.
- Arakawa, A., and V. R. Lamb (1977), Computational design of the UCLA general circulation model, *Meth. Comput. Phys.*, *17*, 174–267.
- Barabash, S., A. Fedorov, R. Lundin, and J.-A. Sauvaud (2007), Martian atmospheric erosion rates, *Science*, *315*, 501–503, doi:10.1126/science.1134258.
- Brain, D., et al. (2010), A comparison of global models for the solar wind interaction with Mars, *Icarus*, *206*, 139–151.
- Bougher, S. W., S. Engel, D. P. Hinson, and J. R. Murphy (2004), MGS Radio Science electron density profiles: Interannual variability and implications for the Martian neutral atmosphere, *J. Geophys. Res.*, *109*, E03010, doi:10.1029/2001GL012884.
- Bougher, S. W., S. Engel, R. G. Roble, and B. Foster (1999), Comparative terrestrial planetary thermospheres. 2. Solar cycle variation of global structure and winds at equinox, *J. Geophys. Res.*, *104*, 16,591–16,611, doi:10.1029/1998JE001019.
- Bougher, S. W., S. Engel, R. G. Roble, and B. Foster (2000), Comparative terrestrial planetary thermospheres. 3. Solar cycle variation of global structure and winds at solstices, *J. Geophys. Res.*, *104*, 17,669–17,692, doi:10.1029/1999JE001232.
- Brace, L. H., and A. J. Kliore (1991), The structure of the Venus ionosphere, *Space Sci. Rev.*, *55*, 81–163.
- Brecht, S. H., and S. A. Ledvina (2012), Control of ions loss from Mars during solar minimum, *Earth Planet. Space*, *64*, 165–178.
- Carlsson, E., et al. (2006), Mass composition of the escaping plasma at Mars, *Icarus*, *182*, 320.
- Dubinin, E., et al. (2008), Plasma environment of Mars as observed by simultaneous MEX-ASPERA-3 and MEX-MARSIS observations, *J. Geophys. Res.*, *113*, A10217, doi:10.1029/2008JA013355.
- Duru, F., D. A. Gurnett, R. A. Frahm, J. D. Winningham, D. D. Morgan, and G. G. Howes (2009), Steep, transient density gradients in the Martian ionosphere similar to the ionopause at Venus, *J. Geophys. Res.*, *114*, A12310, doi:10.1029/2009JA014711.
- Duru, F., D. A. Gurnett, D. D. Morgan, J. D. Winningham, R. A. Frahm, and A. F. Nagy (2011), Nightside ionosphere of Mars studied with local electron densities: A general overview and electron density depressions, *J. Geophys. Res.*, *116*, A10316, doi:10.1029/2011JA016835.
- Elphic, R. C., H. G. Mayr, R. F. Theis, L. H. Brace, K. L. Miller, and W. C. Knudsen (1984), Nightward ion flow in the Venus ionosphere—Implications of momentum balance, *Geophys. Res. Lett.*, *11*, 1007.
- Fillingim, M. O., R. J. Lillis, S. L. England, L. M. Peticolas, D. A. Brain, J. S. Halekas, C. Paty, D. Lummerzheim, and S. W. Bougher (2012), One wind-driven electrojets at magnetic cusps in the nightside ionosphere of Mars, *Earth Planets Space*, *64*, 93–103.
- Fillingim, M. O., L. M. Peticolas, R. J. Lillis, D. A. Brain, J. S. Halekas, D. Lummerzheim, and S. W. Bougher (2010), Localized ionization patches in the nighttime ionosphere of Mars and their electrodynamic consequences, *Icarus*, *206*, 112–119.
- Fjeldbo, G., and R. von Eshleman (1968), The atmosphere of Mars analyzed by integral inversion of the Mariner IV occultation data, *Planet. Space Sci.*, *16*, 1035–1059.
- Forget, F., F. Hourdin, R. Fournier, C. H., and O. Talagrand (1999), Improved general circulation models of the Martian atmosphere from the surface to above 80 km, *J. Geophys. Res.*, *104*, 24,155–24,175, doi:10.1029/1999JE001025.
- Forget, F., R. M. Haberle, F. Montmessin, B. Levrard, and J. W. Head (2006), Formation of glaciers on Mars by atmospheric precipitation at high obliquity, *Science*, *311*, 368.
- Forget, F., E. Millour, K. Dassas, C. Hourdin, F. Hourdin, Y. Wanherdrick, and G. Davis (2007), User manual for the LMD Martian atmospheric general circulation model.
- Forget, F., F. Montmessin, J.-L. Bertaux, F. Gonzalez-Galindo, S. Lebonnois, E. Quémerais, A. Réberac, E. Dimarellis, and M. A. López-Valverde (2009), Density and temperatures of the upper Martian atmosphere measured by stellar occultations with Mars Express SPICAM, *J. Geophys. Res.*, *114*, E01004, doi:10.1029/2008JE003086.
- Forget, F., R. Wordsworth, E. Millour, J.-B. Madeleine, L. Kerber, J. Leconte, E. Marcq, and R. M. Haberle (2013), 3D modelling of the early Martian climate under a denser CO₂ atmosphere: Temperatures and CO₂ ice clouds, *Icarus*, *222*, 81–99.
- Fox, J. L. (1997), Upper limits to the outflow of ions at Mars: Implications for atmospheric evolution, *Geophys. Res. Lett.*, *24*, 2901–2904, doi:10.1029/97GL52842.
- Fox, J. L. (2003), Effect of H₂ on the Martian ionosphere: Implications for atmospheric evolution, *J. Geophys. Res.*, *108*(A6), 1223, doi:10.1029/2001JA000203.
- Fox, J. L. (2004), Response of the Martian thermosphere/ionosphere to enhanced fluxes of solar soft X rays, *J. Geophys. Res.*, *109*, A11310, doi:10.1029/2004JA010380.

- Fox, J. L., and F. M. Bakalian (2001), Photochemical escape of atomic carbon from Mars, *J. Geophys. Res.*, *106*(28), 785–28,795.
- Fox, J. L., and A. Dalgarno (1979), Ionization, Luminescence, and Heating of the upper atmosphere of Mars, *J. Geophys. Res.*, *84*, 7316.
- Fox, J. L., and A. J. Weber (2012), MGS electron density profiles: Analysis and modeling of peak altitudes, *Icarus*, *221*, 1002–1019.
- Fränz, M., E. Dubinin, E. Nielsen, J. Woch, S. Barabash, R. Lundin, and A. Fedorov (2010), Transterminator ion flow in the Martian ionosphere, *Planet. Space Sci.*, *58*, 1442–1454.
- Girazian, Z., and P. Withers (2013), The dependence of peak electron density in the ionosphere of Mars on solar irradiance, *Geophys. Res. Lett.*, *40*, 1960–1964, doi:10.1002/grl.50344.
- González-Galindo, F., M. A. López-Valverde, M. Angelats i Coll, and F. Forget (2005), Extension of a Martian general circulation model to thermospheric altitudes: UV heating and photochemical models, *J. Geophys. Res.*, *110*, E09008, doi:10.1029/2004JE002312.
- Gonzalez-Galindo, F., F. Forget, M. A. López-Valverde, M. Angelats i Coll, and E. Millour (2009a), A ground-to-exosphere Martian circulation model: 1 Seasonal, diurnal and solar cycle variation of thermospheric temperatures, *J. Geophys. Res.*, *114*, E04001, doi:10.1029/2008JE003246.
- Gonzalez-Galindo, F., F. Forget, M. A. López-Valverde, and M. Angelats i Coll (2009b), A ground-to-exosphere Martian circulation model: 2 Atmosphere during solstice conditions – Thermospheric polar warming, *J. Geophys. Res.*, *114*, E08004, doi:10.1029/2008JE003277.
- González-Galindo, F., J.-Y. Chaufray, M. A. López-Valverde, G. Gilli, F. Forget, F. Leblanc, R. Modolo, S. Hess, and M. Yagi (2013), Three-dimensional Martian ionosphere model: I. The photochemical ionosphere below 180 km, *J. Geophys. Res. Planets*, *118*, 2105–2123, doi:10.1002/jgre.20150.
- Gurnett, D. A., et al. (2008), An overview of radar soundings of the Martian ionosphere from the Mars Express spacecraft, *Adv. Space Res.*, *41*, 1335–1346.
- Gurnett, D. A., D. D. Morgan, F. Duru, F. Akalin, J. D. Wittingham, R. A. Frahm, E. Dubinin, and S. Barabash (2010), Large density fluctuations in the Martian ionosphere as observed by the Mars Express radar sounder, *Icarus*, *206*, 83–94.
- Haider, S. A., K. K. Mahajan, and E. Kallio (2011), Mars ionosphere: A review of experimental results and modeling studies, *Rev. Geophys.*, *49*, RG4001, doi:10.1029/2011RG000357.
- Hanson, W. B., and G. P. Mantas (1988), Viking electron temperature measurements: Evidence for a magnetic field in the Martian ionosphere, *J. Geophys. Res.*, *93*, 7538–7544, doi:10.1029/JA093iA07p07538.
- Hanson, W. B., S. Satani, and D. R. Zuccaro (1977), The Martian ionosphere as observed by the Viking retarding potential analyzers, *J. Geophys. Res.*, *82*, 4351–4363, doi:10.1029/J082i028p04351.
- Hourdin, F. (2005), La représentation du transport direct et inverse dans les modèles globaux de climat et l'étude des couplages entre composition et dynamique atmosphérique sur Titan, Habilitation à Diriger des Recherches.
- Hourdin, F. (2010), Intégration des équations de Saint-Venant avec LMDZ, Laboratoire de Météorologie Dynamique, Technical note.
- Hourdin, F., and A. Armengaud (1998), The use of finite-volume methods for atmospheric advection of trace species. Part I: Test of various formulations in a general circulation model, *Mon. Weather Rev.*, *127*, 822–837.
- Keating, G. M., M. Theriot, and S. Bougher (2008), The thermosphere and exosphere of Mars, DPS meeting #40, #6.08, *Bull. Am. Astron. Soc.*, *40*, 397.
- Kopf, A. J., D. A. Gurnett, D. D. Morgan, and D. L. Kirchner (2008), Transient layers in the topside ionosphere of Mars, *Geophys. Res. Lett.*, *35*, L17102, doi:10.1029/2008GL034948.
- Krasnopolsky, V. A. (2002), Mars' upper atmosphere and ionosphere at low, medium and high solar activities: Implication for evolution of water, *J. Geophys. Res.*, *107*(E12), 5128, doi:10.1029/2001JE001809.
- Krasnopolsky, V. A., and P. D. Feldman (2001), Detection of molecular hydrogen in the atmosphere of Mars, *Science*, *294*, 1914.
- Lefevre, F., and F. Forget (2009), Observed variations of methane on Mars unexplained by known atmospheric chemistry and physics, *Nature*, *460*, 720.
- Lefevre, F., S. Lebonnois, F. Montmessin, and F. Forget (2004), Three-dimensional modeling of ozone on Mars, *J. Geophys. Res.*, *109*, E07004, doi:10.1029/2004JE002268.
- Lewis, R. S., M. Collins, P. Read, F. Forget, F. Hourdin, R. Fournier, C. Hourdin, O. Talagrand, and J.-P. Huot (1999), A climate database for Mars, *J. Geophys. Res.*, *104*, 24,177–24,194, doi:10.1029/1999JE001024.
- Luhmann, J. G., and T. E. Cravens (1991), Magnetic fields in the ionosphere of Venus, *Space Sci. Rev.*, *55*, 201–274.
- Lundin, R., S. Barabash, M. Holmström, H. Nilsson, M. Yamauchi, M. Fraenz, and E. M. Dubinin (2008), A comet-like escape of ionospheric plasma from Mars, *Geophys. Res. Lett.*, *35*, L18203, doi:10.1029/2008GL034811.
- Ma, Y., A. F. Nagy, I. V. Sokolov, and K. C. Hansen (2004), Three-dimensional, multispecies, high spatial resolution MHD studies of the solar wind interaction with Mars, *J. Geophys. Res.*, *109*, A07211, doi:10.1029/2003JA010367.
- Madeleine, J.-B., F. Forget, E. Millour, L. Montabone, and M. J. Wolff (2011), Revisiting the radiative impact of dust on Mars using the LMD Global Climate Model, *J. Geophys. Res.*, *116*, E11010, doi:10.1029/2011JE003855.
- Matta, M., P. Withers, and M. Mendillo (2013), The composition of Mars' topside ionosphere: Effects of hydrogen, *J. Geophys. Res. Space Physics*, *118*, 2681–2693, doi:10.1002/jgra.50104.
- McDunn, T. L., S. W. Bougher, J. Murphy, M. D. Smith, F. Forget, J.-L. Bertaux, and F. Montmessin (2010), Simulating the density and thermal structure of the middle atmosphere (~80–130 km) of Mars using the MGCM-MTGCM: A comparison with MEX/SPICAM observations, *Icarus*, *206*, 5.
- Mendillo, M., A. Lollo, P. Withers, M. Matta, M. Pätzold, and S. Tellman (2011), Modelling Mars' ionosphere with constraints from same-day observations by Mars Global Surveyor and Mars Express, *J. Geophys. Res.*, *116*, A11303, doi:10.1029/2011JA016865.
- Miller, K. L., and R. C. Whitten (1991), Ion dynamics in the Venus ionosphere, *Space Sci. Rev.*, *55*, 165–199.
- Modolo, R., G. M. Chantour, E. Dubinin, and A. P. Matthews (2005), influence of the solar EUV flux on the Martian plasma environment, *Ann. Geophys.*, *23*, 433–444.
- Montmessin, F., T. Fouchet, and F. Forget (2005), Modeling the annual cycle of HDO in the Martian atmosphere, *J. Geophys. Res.*, *110*, E03006, doi:10.1029/2004JE002357.
- Morgan, D. D., D. A. Gurnett, D. L. Kirchner, J. L. Fox, E. Nielsen, and J. J. Plaut (2008), Variation of the Martian ionospheric electron density from Mars Express radar soundings, *J. Geophys. Res.*, *113*, A09303, doi:10.1029/2008JA013313.
- Nagy, A. F., et al. (2004), The plasma environment of Mars, *Space Sci. Rev.*, *111*, 33–114.
- Najib, D., A. F. Nagy, G. Toth, and Y. Ma (2011), Three-dimensional, multifluid, high spatial resolution MHD model studies of the solar wind interaction with Mars, *J. Geophys. Res.*, *116*, A05204, doi:10.1029/2010JA016272.
- Němec, F., D. D. Morgan, D. A. Gurnett, F. Duru, and V. Truhlík (2011a), Dayside ionosphere of Mars: Empirical model based on data from the MARSIS instrument, *J. Geophys. Res.*, *116*, E07003, doi:10.1029/2010JE003789.
- Němec, F., D. D. Morgan, D. A. Gurnett, and D. A. Brain (2011b), Areas of enhanced ionization in the deep nightside ionosphere of Mars, *J. Geophys. Res.*, *116*, E06006, doi:10.1029/2011JE003804.

- Nicholson, W. P., G. Gronoff, J. Liliensten, A. D. Aylward, and C. Simon (2009), A fast computation of the secondary ion production in the ionosphere of Mars, *Mon. Not. R. Astron. Soc.*, *400*, 369–382.
- Nier, A. O., and M. B. McElroy (1977), Composition and structure of Mars' upper atmosphere: Results from the neutral mass spectrometers on Viking 1 and 2, *J. Geophys. Res.*, *82*, 4341–4349, doi:10.1029/J5082i028p04341.
- Pätzold, M., S. Tellmann, B. Häusler, D. Hinson, R. Schaa, and G. L. Tyler (2005), A sporadic third layer in the ionosphere of Mars, *Science*, *5749*, 837–839.
- Ridley, A. J., Y. Deng, and G. Tóth (2006), The global ionosphere-thermosphere model, *J. Atmos. Sol. Terr. Phys.*, *68*, 839–864.
- Rohrbaugh, R. P., J. S. Nisbet, E. Bleuler, and J. R. Herman (1979), The effect of energetically produced O_2^+ on the ion temperatures of the Martian thermosphere, *J. Geophys. Res.*, *84*, 3327–3338, doi:10.1029/JA084iA07p03327.
- Sadourny, R. (1975), The dynamics of finite-difference models of the shallow-water equations, *J. Atmos. Sci.*, *32*, 680.
- Sadourny, R., and K. Laval (1984), January and July performance of the LMD general circulation model, in *New Perspectives in Climate Modeling*, edited by A. Berger and C. Nicolis, pp. 173–197, Elsevier, Amsterdam.
- Sánchez-Cano, B., S. M. Radicella, M. Herraiz, O. Witasse, and G. Rodríguez-Caderot (2013), NeMars, an empirical model of the Martian dayside ionosphere based on Mars Express MARSIS data, *Icarus*, *225*, 236–247.
- Schunk, R. W., and A. F. Nagy (2009), *Ionospheres: Physics, plasma physics, and chemistry*, Cambridge Univ. Press, New York.
- Shinagawa, H., and T. E. Cravens (1992), The ionospheric effects of a weak intrinsic magnetic field at Mars, *J. Geophys. Res.*, *97*, 1027.
- Shinagawa, H., and T. E. Cravens (1989), A one-dimensional multispecies magnetohydrodynamic model of dayside ionosphere of Mars, *J. Geophys. Res.*, *94*, 6506–6516, doi:10.1029/JA094iA06p06506.
- Spiga, A., and F. Forget (2009), A new model to simulate the Martian mesoscale and microscale atmospheric circulation: Validation and first results, *J. Geophys. Res.*, *114*, E02009, doi:10.1029/2008JE003242.
- Stewart, A. I., C. A. Barth, C. W. Hord, and A. L. Lane (1972), Mariner 9 ultraviolet spectrometer experiment: Structure of Mars' upper atmosphere, *Icarus*, *17*, 469–474.
- Vailleille, A., V. Tenishev, S. W. Bougher, M. R. Combi, and A. F. Nagy (2009a), Three-dimensional study of Mars upper thermosphere/ionosphere and hot oxygen corona: 1. General description and results at equinox for solar low conditions, *J. Geophys. Res.*, *114*, E11005, doi:10.1029/2009JE003388.
- Vailleille, A., M. R. Combi, S. W. Bougher, V. Tenishev, and A. F. Nagy (2009b), Three-dimensional study of Mars upper thermosphere/ionosphere and hot oxygen corona: 2. Solar cycle, seasonal variations, and evolution over history, *J. Geophys. Res.*, *114*, E11006, doi:10.1029/2009JE003389.
- Van Leer, B. (1977), Towards the ultimate conservative difference scheme. Part IV: A new approach to numerical conservation, *J. Comput. Phys.*, *32*, 101–136.
- Witasse, O., T. Cravens, M. Mendillo, J. Moses, A. Kliore, A. F. Nagy, and T. Breus (2008), Solar system ionospheres, *Space Sci. Rev.*, *139*, 235.
- Withers, P. (2009), A review of observed variability in dayside ionosphere of Mars, *Adv. Space Res.*, *44*, 277–307, doi:10.1016/j.asr.2009.04.027.
- Withers, P., et al. (2012a), A clear view of the multifaceted dayside ionosphere of Mars, *Geophys. Res. Lett.*, *39*, L18202, doi:10.1029/2012GL053193.
- Withers, P., M. O. Fillingim, R. J. Lillis, B. Häusler, D. P. Hinson, G. L. Tyler, M. Pätzold, K. Peter, S. Tellman, and O. Witasse (2012b), Observations of the nightside ionosphere of Mars by the Mars Express Radio Science Experiment (MaRS), *J. Geophys. Res.*, *117*, A12307, doi:10.1029/2012JA018185.
- Woodsworth, R., F. Forget, E. Millour, J. W. Head, J.-B. Madeleine, and B. Charnay (2012), Global modelling of the early Martian climate under a denser CO_2 atmosphere: Water cycle and ice evolution, *Icarus*, *222*, 1–19, doi:10.1016/j.icarus.2012.09.036.
- Yagi, M., F. Leblanc, J.-Y. Chaufray, F. Gonzalez-Galindo, S. Hess, and R. Modolo (2012), Mars exospheric thermal and non-thermal components: Seasonal and local variations, *Icarus*, *221*, 682–693, doi:10.1016/j.icarus.2012.07.022.
- Zhang, M. H. G., J. L. Luhmann, and A. J. Kliore (1990), An observational study of the nightside ionospheres of Mars and Venus with radio occultation methods, *J. Geophys. Res.*, *95*, 17,095–17,102, doi:10.1029/JA095iA10p17095.
- Zou, H., R. J. Lillis, J. S. Wang, and E. Nielsen (2011), Determination of seasonal variations in the Martian neutral atmosphere from observations of ionospheric peak height, *J. Geophys. Res.*, *116*, E09004, doi:10.1029/2011JE003833.